ÉCOLE POLYTECHNIQUE
FÉDÉRALE DE LAUSANNE

LABORATOIRE DES MATERIAUX
SEMICONDUCTEURS

Optical characterization of Molecular Beam Epitaxy grown GaAs nanotrees

by

Oscar Garcia Garcia

submitted to obtain the

BACHELOR'S DEGREE ON ENGINEERING PHYSICS

at

UNIVERSITAT POLITÈCNICA DE CATALUNYA

First supervisor: Prof. Dr. Anna Fontcuberta i Morral
École Polytechnique Fédérale de Lausanne

Second supervisor: Prof. Dr. Ramón Alcubilla González
Universitat Politècnica de Catalunya

Contact details:

Oscar Garcia Garcia
oscargarciag71@gmail.com

Prof. Anna Fontcuberta i Morall
École Polytechnique Fédérale de Lausanne
Laboratoire des matériaux semiconducteurs (LMSC)
MXC - 330
1015 Lausanne
anna.fontuberta-moral@epfl.ch

Prof. Ramón Alcubilla González
Universitat Politècnica de Catalunya
Enginyeria electrònica
C4 - 203. Campus Nord.
08304 Barcelona
ramon.alcubilla@upc.edu

Abstract

In the aim to grow vertical self-catalyzed *GaAs* nanowires on [100] *Si*, a fancy structures with a tapered shape resembling a tree were observed. They were called nanotrees. This is the first time that vertical growth has been achieved without catalyzer in this conditions. However, TEM studies revealed that crystalline structure is not following $\{100\}$ planes, but a more complex disposition that leads to an overall vertical growth. Due to the complexity of this structure, the triggering of the nanotree growth is a random process and for this reason they do not appear in a high yield. It was found out that the growth conditions play an important role to increase the yield, which is currently around 7 %. To assess the optoelectronical properties of this nanotrees, different techniques were used. Raman spectroscopy showed peaks corresponding to zinc-blende, in good accordance with TEM images. Furthermore, surface mode peaks were observed due to the reduced dimensions of the nanotree. Photoluminescence spectroscopy measured the main exciton peak for *GaAs*, as well as another small peak that was attributed to carbon contamination. Cathodoluminescence linked the emission signal to specific parts of the nanotree, revealing a decrease in the intensity due to a defect located in the longitudinal axis of the nanotree. Computational models showed that nanotrees properly confine incident light, opening a range of possibilities in optoelectronic devices. An overview of this possibilities for future devices with nanotrees, which span from energy harvesting to quantum photonics, is presented. Overall, nanotrees are promising nanostructures but their application is limited by the low yield in which they appear.

Acknowledgements

I would first like to express my very profound gratitude to professor Anna Fontcuberta. She gave me the opportunity to work in one of the world's leading labs in nanotechnology. I really appreciate the experience she allowed me to live and I will keep it for life. Her guidance through the project was indispensable for the success of it.

Secondly, I would like to show my gratefulness to Lucas Güniat, to whom I am clearly in debt for sharing his expertise with me. His patience, motivation and immense knowledge helped me to improve day by day.

I would also like to thank Elias Stutz, Luca Francaviglia, Akshay Balgarkashi and Sara Martí for their technical support and their uninterested help.

Finally, I must express my gratitude to the rest of LMSC members, which have welcomed me and gave me the opportunity to join their team.

Contents

List of Abbreviations

MBE	**M**olecular **B**eam **E**pitaxy
VLS	**V**apor **L**iquid **S**solid
SEM	**S**canning **E**lectron **M**icroscope
QD	**Q**uantum **D**ot
HSQ	**H**ydrogen **S**iles**Q**uioxane
E-beam	**E**lectron **beam**
TMAH	**T**etra**M**etil**A**monium **H**ydroxide
RIE	**R**eactive **I**on **E**tching
IPA	**I**so**P**ropyl **A**lcohol
HF	**H**ydrogen **F**luoride
BHF	**B**uffered **H**ydrogen **F**luoride
RHEED	**R**eflection **H**igh-**E**nergy **E**lectron **D**iffraction
TEM	**T**ransmission **E**lectron **M**icroscope
STEM	**S**canning **T**ransmission **E**lectron **M**icroscope
HAADF	**H**igh-**A**ngle **A**nnular **D**ark-**F**ield
FIB	**F**ocused **I**on **B**eam
TO	**T**ransversal **O**ptical
LO	**L**ongitudinal **O**ptical
SO	**S**urface **O**ptical
PL	**P**hoto**L**uminescence
CL	**C**athodo**L**uminescence
RT	**R**oom **T**emperature
LT	**L**ow **T**emperature
FWHM	**F**ull **W**idth **H**alf **M**aximum
ITO	**I**ndium **T**in **O**xide
FDTD	**F**inite **D**ifference **T**ime **D**omain
TFSF	**T**otal-**F**ield **S**cattered-**F**ield
PML	**P**erfectly **M**atching **L**ayer

"Science sans conscience n'est que ruine de l'âme."

Chapter 1

Introduction

1.1 Motivation

An ever increasing world population demands science to concern about sustainability. Step by step, humankind becomes aware that earth can not be exploited indefinitely and that human activity has a big footprint on the environment. Science can play a major role in a development towards an equitable world, providing sustainable solutions and alternatives to current industry. Particularly, nanotechnology opens a wide range of new perspectives in the field of energy production and harvesting, as well as in optimization of resources due to the enhancement of material properties at nano scale.

III-V semiconductors offer, due to their high carrier mobility and direct bandgap, a great potential for optoelectronic applications, from transistors to emitting diodes, and specially for solar cells. However, III-V are scarce and their use should be very well assessed. To reduce the amount of III-V material used, a deposition over a substrate can be done. Using Molecular Beam Epitaxy (MBE), a III-V thin film can be easily grown on a Si wafer. Though, many defects appear due to lattice mismatch. An alternative to thin films can be found in nanowires.

Nanowires are elongated nanostructures with a reduced diameter, about hundreds of nanometers. When grown on a Si substrate, they show a strain relaxation at the interface due to their reduced cross-section, which leads to overcome lattice mismatch. Furthermore, nanowires can be tuned to show desired optoelectronic properties by combining different crystalline layers and thus obtaining different quantum confined structures, as reviewed in [1]. The capability to host these customized quantum structures makes nanowires an ideal support to build functional devices. Applications of nanowires are wide. Krogstrup *et al* demonstrated in [2] the potential of $GaAs$ single nanowire solar cells, achieving outstanding efficiencies due an enhanced absorption promoted by light confinement inside the nanowire. Infrared nanolasers were constructed by Saxena *et al* using a core-shell $GaAs$-$AlGaAs$ nanowire acting as a Fabry-Pérot resonating cavity [3]. Not only in optical applications, Frolov *et al* demonstrated that nanowires can be the perfect platform to host spin q-bits for quantum computing [4]. However, the integration of all these functional devices cited above with current industry is not trivial and further work needs to be developed.

1.2 Objectives and preliminary work

Silicon based technologies commonly use [100] wafers. The present work aims to build III-V nanowires, particularly *GaAs* nanowires, on [100] *Si* in order to obtain procedures compatible with the current industry. The growth of the nanowires is made through Vapor-Liquid-Solid (VLS). In this technique, precursor droplets are placed on the substrate. This precursor contains the core components of the nanowire, III-V elements, and typically gold acting as a catalyzer [5]. Gold nanoparticles, which act as a seed, are useful to tune the nanowire characteristics, such as its diameter and growth direction [6]. However, the presence of gold creates deep-level traps in the *Si* wafer that makes gold-catalyzed VLS incompatible with silicon industry. For this reason, "self-catalyzed" method is purposed, where the precursor droplet only contains III-V elements and the nanowire characteristics are tuned through the substrate and the droplet configuration, as it will be seen below. Self-catalyzed method is not fully understood and having a stable growth is still a challenge.

Previous works using this procedure are shown in figure 1.1. As it can be seen, mostly tilted structures appear, due to the preferential *GaAs* growth direction [111]. However, other more complex structures can be seen, forming a triangular shape called nanotree. This is the evidence that epitaxial growth in [100] direction can be obtained with a self-catalyzed approach, and it is the first time that has been achieved for *GaAs* in [100] *Si*. From now on, the work will be focused in this type of nanowires named nanotrees. Tuning the process characteristics, such as the partial pressure of *As* and *Ga* during Molecular Beam Epitaxy (MBE), more elongated or shortened nanotrees are obtained.

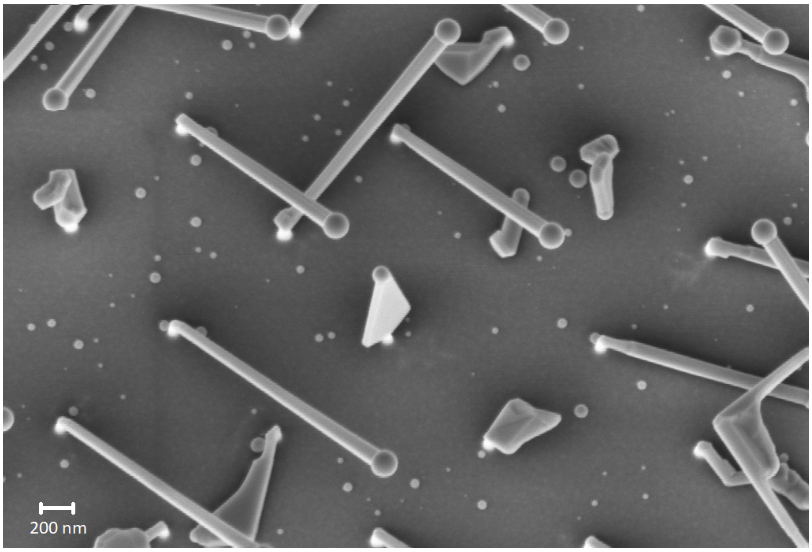

FIGURE 1.1: Scanning Electron Microscope (SEM) image of a self-catalyzed VLS growth where a nanotree can be seen with a brighter tonality in the center. The microscope stage is tilted 20° and rotated 45° to obtain a diagonal view of the nanotree.

Once the nanotree growth procedure is well established, heterostructures will be created by adding subsequent *AlGaAs* and *GaAs* layers. As Maria de la Mata *et al* demonstrated in [1], heterojunctions lead to the creation of quantum confined structures inside the nanowire. This structures are indeed the key to produce functional electronic devices.

Particularly, quantum dots (QD's) are very promising due to their customized optoelectronic properties. Nanowires are a perfect cradle to host quantum dots. Different techniques are known to obtain quantum dots in nanowires, all based on growing subsequent heterojunctions. The ultimate objective of this thesis is to obtain quantum dots. However, the state-of-the-art of this work will take a slightly different approach for growing this structures. Based on what G. E. Cirlin *et al* demonstrated in [7], *InAs* quantum dots can be grown on [100] *Si* by MBE. QD's will be characterized using photoluminescence, expecting an emission peak at around 1.3 μm. Once the existence of QD's is proved, nanotrees will be grown on top of them. Nanotrees will act as a waveguide, extracting the light generated by the quantum dot. Computational models will be used to analyze light propagation inside the nanotree. Based on this simulations, the growth parameters of the nanotree will be tuned to obtain a shape with an optimum light confinement.

However, the control of nanotree growth is still not completely understood. The deposition of the *InAs* quantum dot on the substrate may prevent the triggering of the growth in [100] direction, thus avoiding nanotrees to appear. A part from this method, other more common approaches to obtain quantum dots inside nanotrees will be explored and explained during this work.

Chapter 2

The early life of nanotrees

Several different techniques can be used to obtain nanowires. From a top-down approach, where nanowires are sculpted from a bulk material, to bottom-up approach, where nanowires are grown by epitaxial techniques.

As it is explained in the statement of objectives, this work aims to build vertical nanowires without catalyzer. The gold catalyzer is the key to trigger and control vertical growth in a bottom-up approach. Without catalyzer, other methods to promote vertical growth must be used: pillars. The first part of the process concerns the patterning of *Si* pillars with a top-down approach. A *Ga* droplet deposited on the pillar will act as self-catalyzer and allow vertical growth. Depending on the pillar diameter, the contact angle of the *Ga* droplet changes, and thus the growth characteristics. Therefore, the pillar plays a fundamental role in the vertical growth.

2.1 Pillar patterning

The next lines will describe the pillar patterning process. Figure 2.1 shows an schematic overview of the steps.

Samples are manipulated in a cleanroom where the environment accomplishes purity requirements for nanotechnology [8]. The process starts with a [100] silicon wafer. Firstly, an oxygen plasma is performed with TEPLA 300 plasma stripper to clean and activate the surface before the subsequent processes. A negative resist named HSQ (Hydrogen silsesquioxane) is spin-coated on the wafer to form a very thin coating (step 1). The wafer is loaded in the electron beam lithography system Vistec EBPG5000. E-beam lithography consists in scanning the surface of the material with a focused electron beam in order to activate the resist. With it, very precise drawings can be done, achieving a resolution of even less than 10 nm. E-beam patterning is performed, drawing arrays of circles that will lately become pillars (step 2). Different diameters are tested, from 25 nm to 100 nm, with a pitch distance between each pillar of 1 μm. Markers are also drawn in order to easily identify the pillar arrays when inspected with SEM or optical microscope.

After the e-beam patterning, the resist is developed, this is, the parts that have not reacted are removed with diluted TMAH (Tetramethylammonium hydroxide) (step 3). After, a Reactive Ion Etching (RIE) is performed. This process is a type of dry etching which uses chemically reactive plasma to remove layers from the surface of the wafer. The remaining resist prevents the etching on the circles but not on rest of the surface, thus creating the pillars. It is performed with Adixen AMS200 etcher. The source gases for the plasma are SF_6 and C_4F_8. By using an antenna at radio frequency, molecules in these gases are excited, ionized and dissociated. In this way, a plasma with different species is created. This plasma, which is very reactive, interacts with the surface of the wafer and removes Si layers that are not protected. The process is hold enough time to create pillars of 150 nm high. Subsequently, the sample is bathed in BHF (Buffered Hydrofluoric Acid) to remove the remaining resist. This step is called resist stripping. After the first stripping, a thermal treatment is applied to obtain a silicon oxide layer (step 6). By placing the sample in an atmosphere reach of oxygen and heating it up to 1000° C, the oxidizing agent diffuses into the Si lattice. This forms an amorphous SiO_2 phase. This layer will prevent parasitic growth outside the pillars since Ga shows low affinity to SiO_2 and thus does not deposit on it.

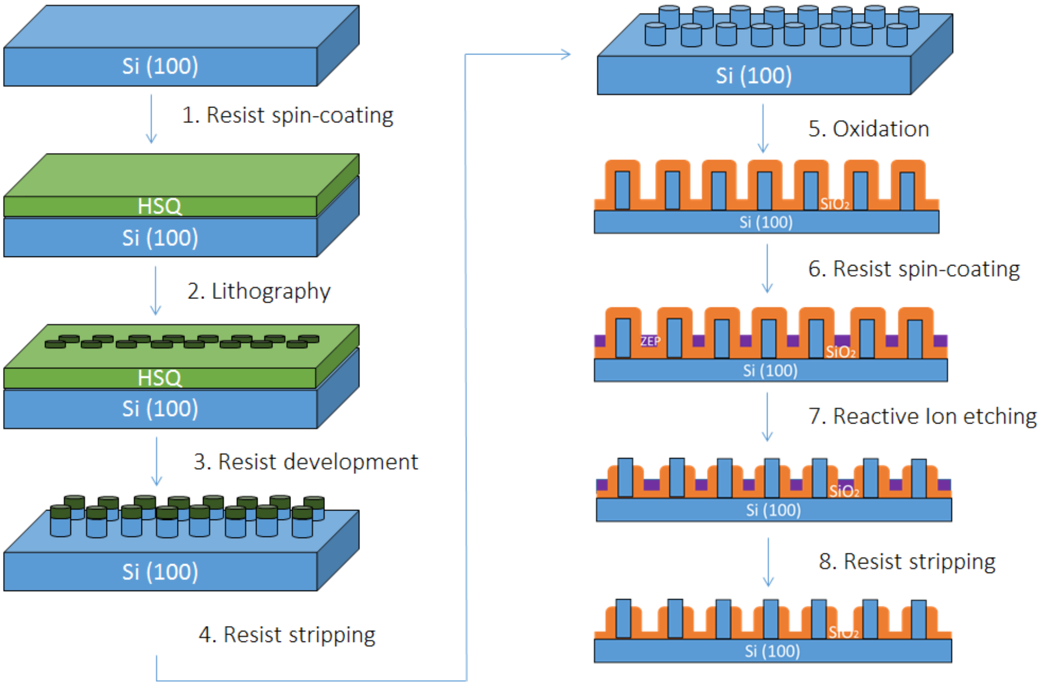

FIGURE 2.1: Process flow for pillar patterning on a Si wafer.

After, a positive resist (ZEP) is spin-coated to a thickness of around 30 nm. This covers the space between the pillars but not the top (Step 6). Then the wafer is heated at 180°C during 5 minutes to activate the positive resist. A RIE is performed in order to eliminate the oxide on top of the pillars, but not the rest of the oxide since it is protected by the resist (Step 7). Now the positive resist is stripped by means of oxygen plasma using TEPLA 300 plasma stripper (Step 8). It works in a similar way than RIE, although in this case, the gas used to create the plasma is O_2. Oxygen plasma etches the resist by turning it into ash and this ash is extracted from the chamber through a vacuum pump. This is why oxygen plasma etching is usually called plasma ashing.

Ulteriorly, the sample is cleaned with a sonication bath, 5 minutes in acetone followed by 1 minute in IPA, both at 60°C. A sonication bath consists of an ultrasonic emitter that creates pressure waves in the media where the sample is located, acetone and IPA in this case. This induces cavitation bubbles that, when collapse, they release a strong vibration into the sample. With it, all traces of contaminants are thoroughly removed.

A last step to remove oxide and obtain a smooth surface on the top of the pillar is taken, etching the sample with an HF bath during 30 seconds. With this process, a thick SiO_2 layer is obtained everywhere, except on top of the pillars, where a thin native oxide layer (around 4 nm) still remains present. The thick oxide layer will prevent droplet deposition, thus allowing growth only on the pillars.

2.2 Molecular beam epitaxy

Crystal growth is achieved with a process named Molecular Beam Epitaxy (MBE). It is a widely used technique for fabrication of semiconductor crystals, mainly at research scale, but also applicable to industry. Particularly, MBE is ideal to grow III-V semiconductors because it allows precise control of the crystal composition with monolayer resolution, achieving high purity defect free growths.

The process occurs in an ultra-high vacuum chamber, at around 10^{-13} bar. Effusion cells, also known as Knudsen cells, heat the materials that will from the crystal, such as gallium and arsenic in a ultra pure form. These materials slowly sublimate, creating a molecular beam towards the center of the chamber. The term "beam" emphasizes the fact that atoms do not interact with each other or with the chamber during the diffusion process due to their high mean free path at that temperature. A substrate is placed inside the vacuum chamber, where it meets the molecular beams created by the effusion cells, as can be seen in figure 2.2. As the atoms reach the substrate, they condensate in an ordered way, forming a crystal. While this process occurs, Reflection High-Energy Electron Diffraction (RHEED) is often used for monitoring the properties of the crystal surface and guarantee a growth with minimum defects.

This is a general and well-known method to grow crystalline structures such as thin films. However, to grow nanowires, a particular technique based on MBE must be used: Vapor-Liquid-Solid.

2.2.1 Vapor - Liquid - Solid

A variant of MBE named Vapor-Liquid-Solid deposition (VLS) is used to achieve epitaxial growth forming nanowires instead of a film. As discussed in the statement of objectives, this technique is based on a deposition of a precursor droplet on the substrate, which will trigger the growth. Usually, the

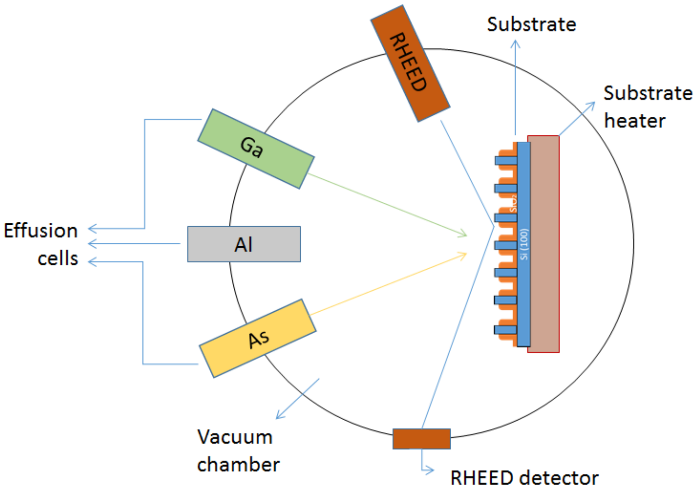

FIGURE 2.2: Scheme of a Molecular Beam Epitaxy chamber with Gallium (*Ga*), Aluminum (*Al*) and Arsenic (*As*) effusion cells.

precursor features, apart from the core components, an element acting as a catalyzer. The most extended catalyzer for this technique is gold. However, gold creates deep-level traps in the *Si* wafer. Deep-level traps are defects in semiconductors that create electronic levels in the middle of the forbidden band. They require a larger energy than dopant levels to extract carriers from them, usually larger than the characteristic thermal energy kT, being k the Boltzmann constant and T the temperature. They act as a non-radiative recombination centers, deteriorating the optoelectronic properties. This growth technique is thus incompatible with silicon based devices. To overcome this problem, "self-catalyzed" method is purposed, where precursor droplets only contains III-V elements. Firstly, the droplet is formed by *Ga* predeposition. Due to its low affinity with SiO_2, *Ga* only condensates on top of the pillars, where the oxide layer is very thin. The role of this droplet is to create a liquid alloy that becomes a preferential side of deposition for *As* and *Ga*, changing from gas to liquid state [9]. When *As* pressure is increased in the chamber, *As* molecules penetrate in the droplet until they reach oversaturation. Eventually, some of this *Ga* and *As* molecules in liquid state attach to the surface of the crystal. Now they have become adatoms. This adatoms migrate and move through the surface until they find a place in the crystal where they can fit, forming subsequent layers.

Preferential *GaAs* growth direction [111] makes tilted nanowires more likely to appear in [100] *Si*. Nevertheless, it has been seen that the droplet size and contact angle play a major role in the triggering of the nanotrees growth. Higher contact angles makes nanotrees more likely to appear. By tuning the pillar diameter and the thickness of the native oxide, an optimum contact angle was found. However, the exact value of this parameters, as well as the growth conditions on the MBE, such as substrate temperature and gas pressures, can not be reveled due to confidentiality agreements. A yield of

7% of nanotrees with respect to [111] tilted wires is obtained.

Figure 2.3 shows some interesting features of the growth. Firstly, side-viewed and face-viewed nanotrees are imaged, as well as the pillars where they are grown. Due to the growth triggering, nanotrees only grow facing this two directions, as it will be discussed in section 2.3. Secondly, tilted nanowires growing in [111] directions are present, besides other strange-shaped crystals that arise from a failed growth. Droplets outside the pillars are sometimes observed, but this is not a problem as far as they do not trigger parasitic growth.

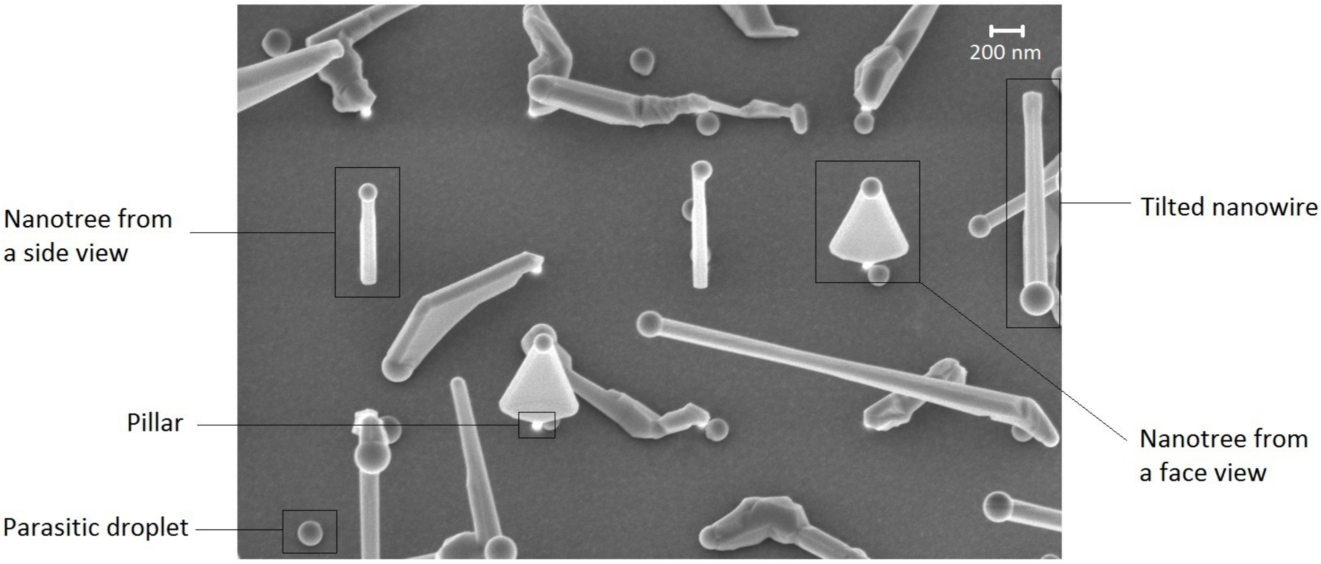

FIGURE 2.3: SEM image that illustrates different results from the growth process. The stage is titled 20° for a more clear view of the nanotrees.

2.3 Birth of nanotrees

This section aims to assess the mechanism that triggers the growth of nanotrees and answer the following question: Why can't we have a 100% yield of nanotrees?

The work presented here was developed by Sara Martí and Jordi Arbiol from Institut Català de Nanociència i Nanotecnologia (ICN2). Images in this section are extracted from their "Report on Nanotree [001] grown *GaAs* nanowires" with their agreement. A nanotree was extracted from the sample and was transferred to a TEM grid following the procedure explained in section 2.4.1. It was analyzed by means of a Transmission Electron Microscope FEI Titan located at Instituto de Nanociencia de Aragón (LMA-INA). Operating in High-Angle Annular Dark-Field (HAADF) mode, atoms with a larger atomic mass are seen brighter than light ones, due to the stronger scattering

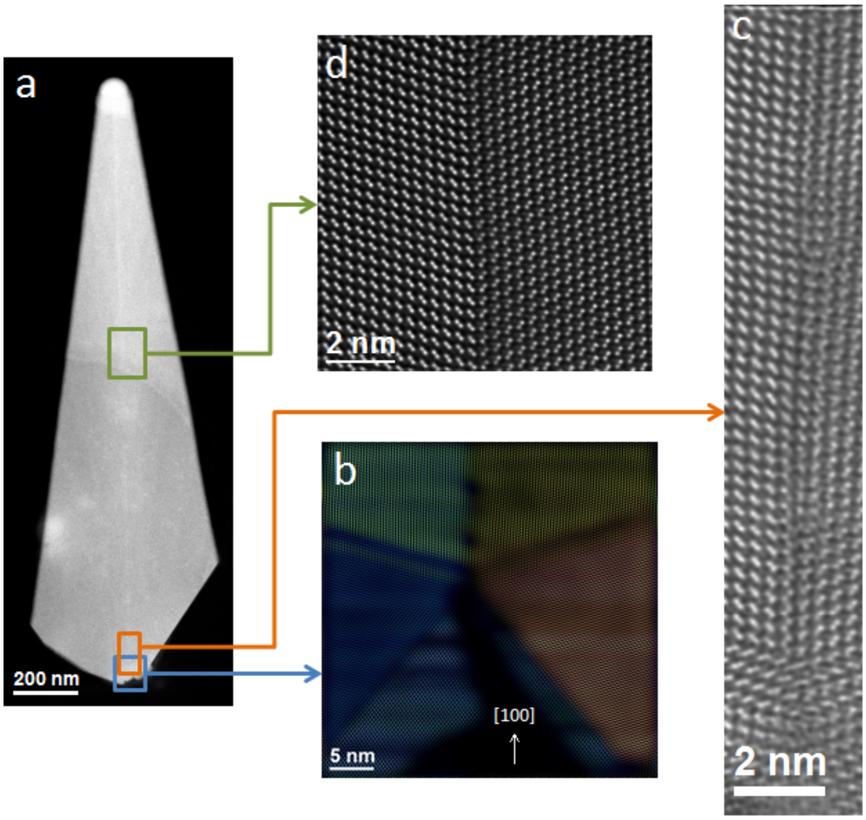

FIGURE 2.4: STEM images obtained by Sara Martí where different twins and defects can be observed at different regions of the nanotree.

that they produce. Interesting features were found concerning the crystalline structure.

Figure 2.4b shows five different crystal domains at the base of the nanotree. The twins between this domains coincide with their $\{111\}$ planes. This is known as a penta-twin and has been reported previously [10] [11].

Here the concept of polarity must be introduced. For $\{111\}$ planes in zincblende, a crystal can be differentiated regarding the order of the molecules that form it. For example, in $GaAs$, it is said to be A-polar if the As comes before the Ga, being the last epitaxial layer of Ga. Aversely, it is said to be B-polar if the last layer is As. In order to complete the penta-twin, a polarity inversion must occur at some point. It was found that this polarity inversion occurs a few monolayers after the twin with the bottom domain, forcing two Ga atomic layers to grow together. This is energetically unfavorable and thus very unlikely to occur, being this the cause that nanotrees appear randomly and a yield of 100% can not be achieved.

The two upper domains, green and yellow in figure 2.4b, extend towards the top of the nanotree. For perfect face-centered cubic tetrahedral subunits, the angle between adjacent $\{111\}$ facets must be 70.53° [12]. However, to complete a 360° penta-twin there is a 7.35° angle deficiency. As a result of this deficiency, a region where the strain is released appears between the two upper domains. This happens immediately above the penta-twin, as it can be seen in figure 2.4c, where stacking faults are present. After this region, which is not longer than 20 nm, no more defects are found apart from the vertical twin, as it can be seen in figure 2.4d.

With this information, it can be understood how the nanotree is formed. Figure 2.5 shows the main steps of the growth. Firstly, a [100] domain grows epitaxially with the [100] *Si* pillar until it shows its $\{111\}$ facets (step 1). At this point, two new domains appear growing from this $\{111\}$ facets. Now, if a polarity inversion occurs at some point, the penta-twin will be completed and the nanotree will form (step 2). When this domains shown again $\{111\}$ planes, which in this case are (111)A and (111)B thanks to the polarity change, the upper domains start growing (step 3). Thus, a nanotree can be understood as two [111] wires growing side by side forming a "fake" [100] direction. Additionally, the fact that all the growth steps follow $\{111\}$ plains explains why the face-side of the nanotrees are always pointing towards [110] directions and not other intermediate positions, as it has been seen previously in figure 2.3.

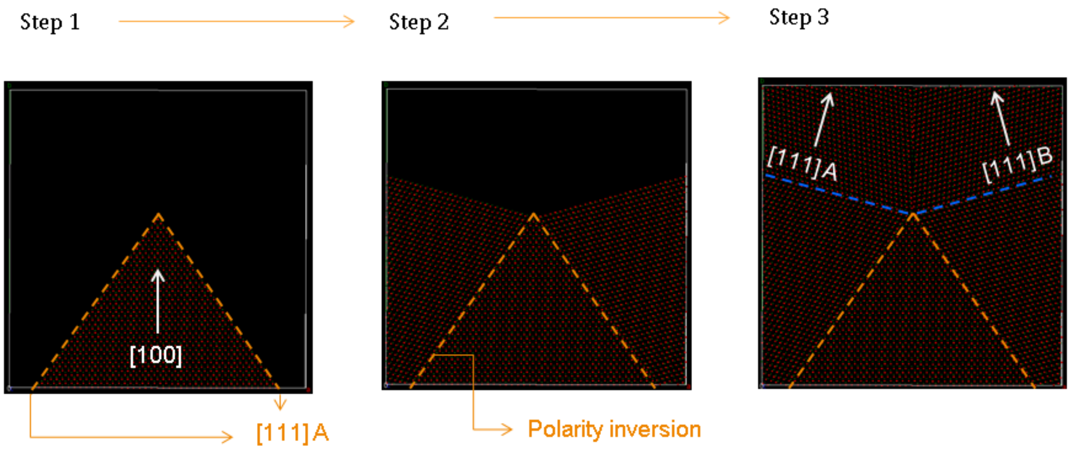

FIGURE 2.5: Diagram of the first steps of the growth of a nanotree. The polarity inversion occurs a few monolayers after the twin with the lower domain, as indicated.

2.4 Manipulation of nanotrees

The objective of this work is to optically characterize the nanotrees. In order to do so, they must be extracted from the array and transferred to another substrate to prevent interferences with the other nanowires during the measurements. Furthermore, the position of the nanotree with respect to the optical setup plays a major role. For example, a laying nanowire maximizes light absorption and thus increases the measured signal. A laying nanotree has also a large surface in contact with the substrate, which maximizes heat transfer. Thanks to this fact, a higher input optical power can be injected on the tree without burning it, which will be useful for Raman spectroscopy. Besides, a laying nanotree with its face-side looking upwards allows to have a two-dimensional map of the composition, which will be useful specially for cathodoluminescence.

Nanotrees are of the order of 1 μm long and grow on pillars of around 40 nm. If observed with an optical microscope, they appear as black dots. SEM is needed to differentiate them from the other nanowires. As the height to base ratio is large, they can be easily detached from the pillars by mechanical force. However, extremely precise techniques must be used to reach the accuracy required to manipulate them. Two different approaches are essayed in this work: micromanipulator and Omniprove.

2.4.1 Micromanipulator

The micromanipulator uses a glass needle mounted in an airbed stage with an optical microscope to operate on the sample. To achieve enough accuracy, the glass needle is submitted to a subsequent melting and stretching process until it reaches a diameter of the order of 1 μm.

As the nanotrees can not be differentiated with an optical microscope, the first step of the procedure is to map the sample with SEM. Once nanotrees are targeted and their positions in the array are known, the optical setup becomes useful. The glass needle is placed in the optical path of the microscope and is focused in its very end. This step is specially critical because of the transparency of the needle and the reduced depth of field of the optical microscope. An accidental contact with the microscope stage may break the needle and damage the sample.

Once the needle is settled in focus, it is stored above the focal point and the sample is approached from the bottom to the focal point of the microscope. Once the sample is in focus, the needle is moved down very slowly until it reaches the sample surface and appears in the focal plane. This procedure ensures that there is no undesired contact between the needle and the sample. Now the needle is moved to the base of the nanotree to crop it. The nanotree thus detaches from the substrate and sticks to the needle by electrostatic forces.

The needle is moved up and the microscope stage is moved down. The new substrate is loaded on the microscope stage and brought to the focal point. Then the needle with the nanotree is moved down to meet the substrate in the focal plane. By gentle tapping the needle, the nanotree will detach and fall into the substrate, sticking on it by electrostatic forces. The nanotree has now been transferred.

A further inspection with SEM may be done in order to know the exact position and orientation of the nanotree on the new substrate. However, the markers on the substrate are useful to have a gross idea of its position.

It was found out that this technique was very selective in the sense that it is easy to extract one particular nanotree without damaging the others, specially if it is in the edge of the array, as it can be seen in the figure 2.6. However, this technique shows a bad reliability in the sense that nanotrees can be easily lost during the process. It is estimated that the time to develop the whole manipulation, including SEM imaging, is around 3 hours.

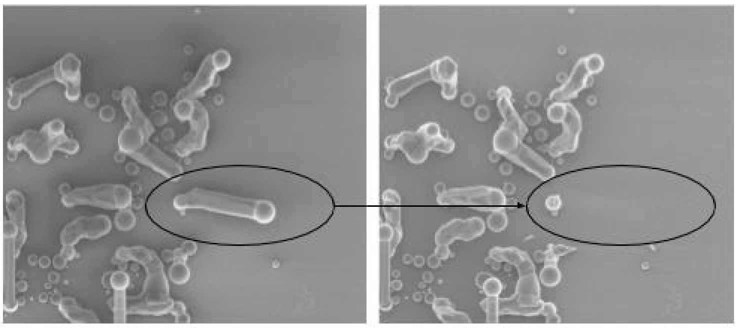

FIGURE 2.6: Micromanipulation of a nanowire sample where selectivity is shown. The nanowire was extracted from the array without damaging its surroundings. The procedure was tested in a nanowire dummy sample before applying it to nanotrees.

2.4.2 SEM/FIB Omniprobe manipulator

A SEM/FIB setup is a very powerful tool for metrology, sputtering and manipulation at micro and nano scale. It consists of a dual column which uses electrons (SEM) and ions (FIB) to bombard the sample. With low beam currents, the FIB column images the surface of the sample. With high beam currents, sputtering or milling can be performed up to a resolution of tenths of nanometers. Furthermore, FEI Nova NanoLab^{TM} 600 DualBeam (FIB/SEM) includes an Omniprobe manipulator and a gas injection system for platinum and insulator deposition [13].

A second approach to overcome manipulation of nanotrees can be found in Omniprobe manipulator. A tungsten needle of around 0.5 μm is used to extract the nanotrees. The procedure holds as follows.

The sample is loaded in the vacuum chamber and observed with SEM to target the nanotrees. The stage is moved to place the sample in the eucentric position, this is, where the electron and ion beams meet, in order to be observed with both imaging systems. The FIB column is at 52° with respect to the SEM column, which allows to have a better space view of the sample and will be very useful during the Omniprobe approach. Afterwards, the Omniprobe needle is inserted in the chamber and approximated to the surface. As the stage movement is much more precise than the Omniprobe movement, it is better to first move the stage down, focus the Omniprobe in the eucentric point and then move the stage up to meet the position. If the needle is not thin enough to reach one single nanotree it can be sharpened using the ion beam in sputtering mode. Once the needle is in contact, the nanotree may attach by electrostatic forces. If this does not happen, a platinum deposition is made. This acts as a welding and attaches the nanotree completely to the needle. When the needle is retracted, the nanotree detaches from the pillar. Then the stage is moved down and the new substrate is placed below the needle. Now, by dragging the needle on the substrate the nanotree is released. If this does not happen, the welding point can be cut with the FIB.

It was found out that this technique, in comparison with the micromanipulator, allowed a good selectivity and a fair reliability. The whole procedure takes around 2 hours and the deposition of the nanotree is more precise. However, the accumulated time under the SEM/FIB beam pollutes the sample with carbon. Besides, traces of tungsten and platinum coming from the needle and the welding respectively may be present. Raman spectroscopy of Omniprobe manipulated nanotrees showed strange peaks that were attributed to this contamination.

Chapter 3

Raman spectroscopy

Thanks to its contact-less nature and micrometer resolution, Raman spectroscopy is an ideal technique for characterization of semiconductor arrangements. With it, information about lattice structure, orientation, strain and size can be obtained. It has been widely used for conventional nanowires in previous works and this chapter aims to extend this analysis to nanotrees.

3.1 Phonons

To understand Raman scattering the concept of phonon must be assessed. Phonons are quantized lattice vibrations in a crystal. From a mass-spring model, it can be deduced that phonons behave as traveling waves. This waves induce a displacement of the atoms in the lattice from their equilibrium position, which is known as vibration.

There is a minimum possible wavelength that can give rise to a phonon, which corresponds to two times the distance between adjacent atoms in the lattice. Any wavelength shorter than this can be mapped into a wavelength longer than $2a$ (with a the length of the primitive cell) due to the periodicity of the lattice. This can be viewed as a satisfaction of the Nyquist sampling theorem, considering that atoms are the sampling points. From a crystallographic approach, this is reflected in the fact that all phonon modes lie inside the first Brillouin zone, which spans from $\frac{-\pi}{a}$ to $\frac{\pi}{a}$. In other words, all physics in a lattice happens inside the Brillouin zone.

After solving a one-dimensional spring-mass problem with alternating masses m_1 and m_2, which stand for the two type of ions in a binary crystal, it can be demonstrated that

$$\omega_{\pm}^2 = K\left(\frac{1}{m_1} + \frac{1}{m_2}\right) \pm K\sqrt{\left(\frac{1}{m_1} + \frac{1}{m_2}\right)^2 - \frac{2(1-\cos(ka))}{m_1 m_2}} \tag{3.1}$$

where K is the spring constant, ω is the angular frequency and k is the wavevector of the vibration [14]. From this result, the dispersion relation, which states the relation between ω and k, can be deduced. The minus sign in the square root from equation 3.1 corresponds to the so-called acoustic modes, in which atoms vibrate together with their adjacent neighbors. For $k \to 0$, it shows a linear relation and $\omega_{-}(0) = 0$. The plus sign corresponds to an optical mode. In it, atoms move out of phase with respect to their neighbors. While one atom moves to the right, its adjacent atom moves to the left. They are called optical modes because they can be excited with light. As deduced from equation 3.1, they show a non-zero frequency but a null derivative for $k = 0$.

However, in a three dimensional crystal, phonons are polarized in a certain direction. If the vibration follows the direction of the wavevector they are called longitudinal modes, while if they have a perpendicular direction they are called transverse modes. As an abbreviation, L and T are used to denote longitudinal and transverse respectively, and A and O mean acoustic and optic, respectively. For example, TO stands for a transverse optical mode. From the degrees of freedom in a three-dimensional lattice, it can be derived that if there are p atoms in the primitive cell, the phonon dispersion relation will have three acoustical modes and $3p - 3$ optical phonon modes. Particularly, *GaAs* zinc-blende holds two atoms per primitive basis, thus having three optical branches and three acoustic branches. In wurtzite *GaAs* there are 4 atoms per primitive basis, leading to total number of 9 optical modes. Figure 3.1 shows schematic GaAs dispersion relation along $\Gamma \rightarrow L$. Black lines correspond to zinc-blende. For wurtzite, the dispersion relation is obtained by folding the one for the zinc-blende. This can be done because the extent of the first Brillouin zone of zinc-blende along [111] is twice the one for wurtzite along [0001] [15]. Note that not all modes are represented in this plot. This is due to the fact that it only covers a certain direction along the Brillouin zone.

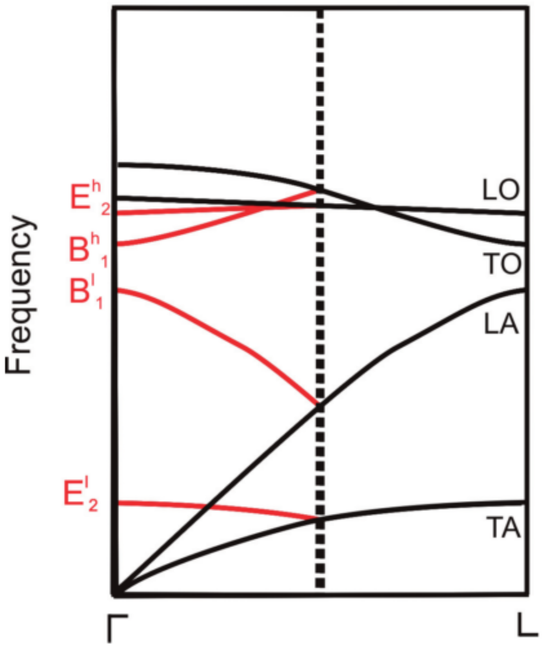

FIGURE 3.1: Phonon dispersion for zinc-blende (black) and wurtzite (black and red) *GaAs*. Extracted and adapted from [15].

3.2 Macroscopic theory of Raman scattering

Light interacting with matter gives rise to different phenomena such as reflection, refraction and absorption. However, in a medium where inhomogeneities are present, another interesting phenomena named scattering can occur. If inhomogeneities are static, such as defects in crystals, photons are re-emitted at the same frequency of the incident light. This particular process is called elastic scattering. If inhomogeneities are dynamic, this is, the material properties change during time, light can be re-emitted at different frequencies, giving rise to inelastic scattering.

Raman scattering is an inelastic scattering with energy and momentum transfer between photons and the scattering material which creates or annihilates a phonon. It can be understood from a classical point of view by considering the polarizability of the material and the radiation of the induced dipole moment at frequencies different from the incident light.

Starting from the electric field of the incident light, which can be expressed as

$$\vec{E} = E_0\, cos(\vec{k_i}\vec{r} - \omega_i t) \tag{3.2}$$

and the displacement of an atom in the lattice, this is, the phonon amplitude

$$\vec{u} = u_0\, cos(\vec{K}\vec{r} - \Omega t) \tag{3.3}$$

The dipole moment induced by an electric field in a material is

$$\vec{P} = \alpha \vec{E} \tag{3.4}$$

Where α is a 3x3 tensor representing the polarizability of the media. Atomic vibrations modify this polarizability and thus α should be expressed as a function of $\vec{u}$. At room temperature, the amplitude of the vibrations is small compared to the lattice constant. Concerning this fact, the relation between the phonon amplitude and the polarizability can be written as a Taylor expansion.

$$\alpha = \alpha_0 + \alpha_1 u + \alpha_2 u^2 + ... \tag{3.5}$$

Where α_n are the corresponding derivatives. Taking the expansion up to first order, equation 3.4 can be written as

$$\begin{aligned} \vec{P} = \alpha_0\, E_0\, cos(\vec{k_i}\vec{r} - \omega_i t) + \frac{1}{2}\alpha_1 E_0 u_0 \cdot \\ \cdot \left[cos((\vec{k_i} + \vec{K})\vec{r} - (\omega_i + \Omega)t) + cos((\vec{k_i} - \vec{K})\vec{r} - (\omega_i - \Omega)t)\right] \end{aligned} \tag{3.6}$$

This expression shows the behavior of the material as incident light of frequency ω_i impinges into it. The first summand of equation 3.6 corresponds to Rayleigh scattering. As it can be seen, the dipole moment frequency does not change from the incident light frequency, and thus the light is re-emitted at the same wavelength, giving rise to an elastic scattering. In the second summand a shift in the frequency can be found. Light is re-emitted at a different frequency due to an inelastic scattering. This is named Raman scattering.

Note that, for an inelastic scattering to occur, the polarizability of the material must be dependent on the vibrations of the lattice. The shift corresponding to an emission of a lower frequency photon is named Stokes shift, while the photon with a higher frequency corresponds to anti-Stokes shift. In a Stokes process, a phonon is created, and thus the emitted photon must have a lower energy in order to satisfy conservation laws. Likewise, in an anti-Stokes process, a phonon is annihilated and the emitted photon acquires larger energy. The probability of an Stokes or anti-Stokes scattering is dependent on the phonon population at a given temperature. For this reason, generally Stokes peaks are more intense and thus they will be the ones studied with the Raman spectrometer. Table 3.1 shows the expected Raman shifts in *GaAs* zinc-blende and wurtzite that can be calculated from the theory explained above, corresponding to phonons at the center of the Brillouin zone. Only phonons at the center of the Brillouin zone can be probed due to their strong dispersion far from this point. The modes that are not present in the table are Raman inactive modes. In this modes, the polarizability of the lattice does not change in time, and thus no Raman shift is expected.

Structure	Mode	Raman shift / cm^{-1}
Zinc-blende	TO	267.7
	LO	291.9
Wurtzite	$A_1(TO)$	267.7
	$A_1(LO)$	291.9
	$E_1(TO)$	267.7
	$E_1(LO)$	291.9
	$A_1(LO)$	291.9
	E_2^h	261.3
	E_2^l	62.1

TABLE 3.1: Expected Raman shifts for bulk *GaAs* in zinc-blende and wurtzite phases.

3.3 Selection rules

As elsewhere, momentum and energy conservation laws hold for Raman processes.

$$\begin{aligned} \omega_i &= \omega_s + \Omega \\ \vec{k}_i &= \vec{k}_s + \vec{K} \end{aligned} \tag{3.7}$$

Thus, it is clear that the direction of the incident light polarization with respect to the crystal is in strong relation with the Raman signal. Depending on the symmetries of the light with respect to the nanotree, some modes will be observed and some will not. The intensity of the scattered radiation can be calculated from the well known time-averaged power radiated by a dipole, expressed as:

$$I_s \propto I_i \, |\hat{e}_i \, \boldsymbol{R} \, \hat{e}_s|^2 \tag{3.8}$$

where I_s and I_i are the intensities of the scattered and incident light, respectively. $\hat{e}_s$ and $\hat{e}_i$ are the polarization unitary vectors for the scattered and incident light, respectively and $\boldsymbol{R}$ is the Raman tensor, which is a second rank tensor defined as $\boldsymbol{R} = \alpha_1 u$.

By assessing the lattice symmetries, most of the components for the Raman tensor can be deduced [16]. For a zinc-blende lattice, Raman tensors expressed in canonical basis can be written as

$$\boldsymbol{R_x} = \begin{bmatrix} 0 & 0 & 0 \\ 0 & 0 & 1 \\ 0 & 1 & 0 \end{bmatrix} \quad \boldsymbol{R_y} = \begin{bmatrix} 0 & 0 & 1 \\ 0 & 0 & 0 \\ 1 & 0 & 0 \end{bmatrix} \quad \boldsymbol{R_z} = \begin{bmatrix} 0 & 1 & 0 \\ 1 & 0 & 0 \\ 0 & 0 & 0 \end{bmatrix} \tag{3.9}$$

Each of this tensors represent an oscillation in a certain direction. By a linear combination of them, phonons in all directions can be expressed. Using this tensors, the selection rules can be derived. However, for the study of the selection rules in nanotrees, it is convenient to change to a basis where the main geometric axis are represented [17]. For a nanotree, the most convenient basis is $\vec{x}' = (0-11)$, $\vec{y}' = (011)$, $\vec{z}' = (-100)$. In this new basis, matrices in equation 3.9 can be expressed as:

$$\begin{gathered} \boldsymbol{R'_x} = \begin{bmatrix} -1 & 0 & 0 \\ 0 & 1 & 0 \\ 0 & 0 & 0 \end{bmatrix} \quad \boldsymbol{R'_y} = \frac{\sqrt{2}}{2} \begin{bmatrix} 0 & 0 & -1 \\ 0 & 0 & -1 \\ -1 & -1 & 0 \end{bmatrix} \\ \boldsymbol{R'_z} = \frac{\sqrt{2}}{2} \begin{bmatrix} 0 & 0 & 1 \\ 0 & 0 & -1 \\ 1 & -1 & 0 \end{bmatrix} \end{gathered} \tag{3.10}$$

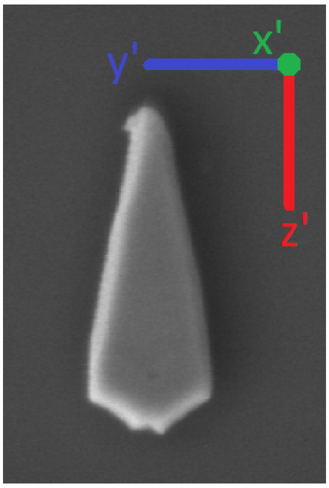

FIGURE 3.2: SEM face-side image of a laying nanotree where the main geometric axis used for Raman spectroscopy are represented.

3.4 Measurements in nanotrees

The optical setup consists of a 532 nm Ti:Shappire laser focused with an objective lens that allows μm resolution. For simplicity, a backscattering geometry will be used. This is, the scattered light is collected in the anti-parallel direction of the incident light. The nanotree is laying on a silicon substrate as it was transfered accordingly to section 2.4. Incident light follows $\vec{x}'$ axis. Although matrices in equation 3.10 are expressed in the convenient geometrical basis, they represent phonons along the main axis of the canonical basis. To obtain the relation between this matrices and their corresponding phonons along the axis of the convenient geometrical basis, a linear combination of them must be taken. For LO modes, which vibrates along $\vec{x}' = (0-11)$, the linear combination to take is:

$$\boldsymbol{R}_{LO} = \frac{1}{\sqrt{2}}(\boldsymbol{R}'_z - \boldsymbol{R}'_y) = \begin{bmatrix} 0 & 0 & 1 \\ 0 & 0 & 0 \\ 1 & 0 & 0 \end{bmatrix} \tag{3.11}$$

And for the TO modes, which are polarized along $\vec{y}' = (011)$ and $\vec{z}' = (-100)$ their respective tensors are

$$\boldsymbol{R}_{TO,y'} = \frac{1}{\sqrt{2}}(\boldsymbol{R}'_y + \boldsymbol{R}'_z) = \begin{bmatrix} 0 & 0 & 0 \\ 0 & 0 & -1 \\ 0 & -1 & 0 \end{bmatrix} \tag{3.12}$$

$$\boldsymbol{R}_{TO,z'} = \boldsymbol{R}'_x = \begin{bmatrix} -1 & 0 & 0 \\ 0 & 1 & 0 \\ 0 & 0 & 0 \end{bmatrix} \tag{3.13}$$

By plugging tensor 3.11 in the intensity equation 3.8 it can be seen that, for this backscattered setup, the intensity of LO mode is zero. In other words, LO is forbidden by the selection rules for any polarization in the $(y' - z')$ plane.

For simplicity and to enhance the collected signal, in the first measurement no particular polarization was chosen for output light. However, since it is collected in the $\vec{x}'$ direction, it must have a polarization lying in the $(y' - z')$ plane . Figure 3.3a shows the results for this measurement for three different incident light polarizations. Firstly, two main peaks are observed at 267 cm^{-1} and at 289 cm^{-1}. Accordingly to table 3.1, this peaks are attributed to TO and LO modes, respectively. Selection rules predict that for this setup no LO modes are active. However, it has been observed previously in nanowires [17]. This is attributed to two things. On one hand, the face-side of the nanotree may not follow exactly $\{110\}$ planes. Due to the fact that it is thinner at the top, it may show higher order planes that allow LO modes in backscattering configuration. On the other hand, due to the strong interaction of light with the material, the Poynting vector changes locally inside the nanotree, exciting phonons that may not follow the incident light direction $\vec{x}'$.

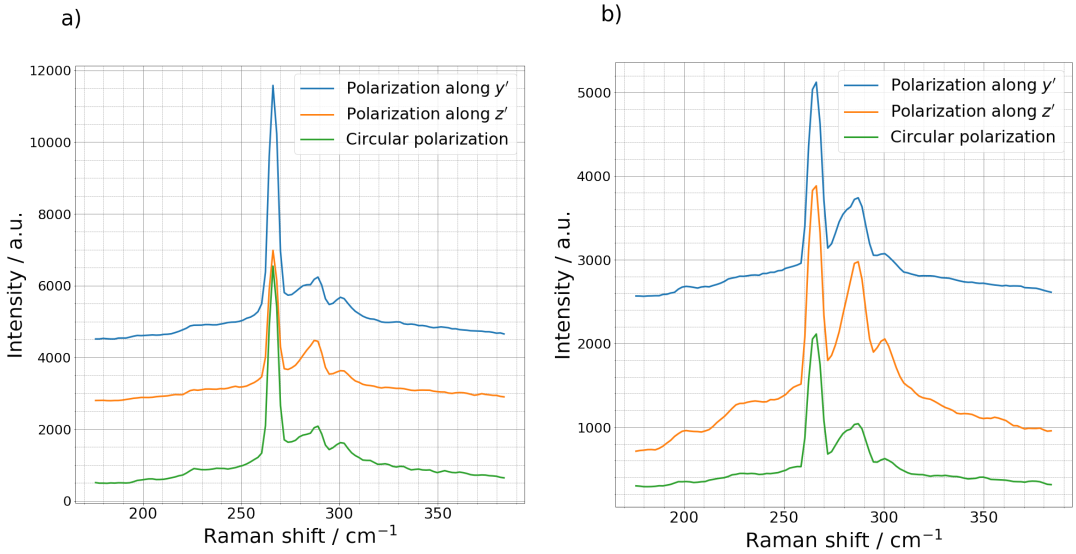

FIGURE 3.3: Raman spectra of measurements with different input polarizations. In plot a) no output polarization is chosen, while in plot b) the output polarization is along z′. Plots are shifted vertically for a better visualization.

The fact that no peak is present around 261.3 cm^{-1} states that there is no wurtzite, thus being only zinc-blende phase, in accordance with the TEM study. The sharpness of the TO mode, with a Full Width Half Maximum (FWHM) of around 6 cm^{-1} shows a fairly good crystalline structure [18]. The LO peak is wider than the TO. The reason for this, according to previous works [19], is the presence of a Surface Optical (SO) peak overlapped with it. In fact, for incident polarization along $\vec{y}'$, a clearly different peak can be seen shifted to the left. This is attributed to a SO mode. Furthermore, the shift of the LO peak with respect to theoretical predictions (291.9 cm^{-1}) is attributed to a heating of the tree due to the laser light, as it is discussed in [19]. In their work, Begum *et al* observed in *GaAs* and *InAs* nanowires a shift towards lower energies of this LO peak proportional to the laser power, which matches perfectly the experimental results presented here. Lastly, the small peak observed at 300 cm^{-1}, as well as the small "step" at 225 cm^{-1} have been observed also away from the nanotree. For this reason, they are attributed to signal from the *Si* substrate or to an artifact created by the optical system.

Figure 3.3b shows the results for a setup where the output polarization was chosen to be along $z' = (-100)$. Selection rules predicted by the Raman tensor in equations 3.12 and 3.13 show that for an output polarization along z', TO mode is only allowed if the input polarization is along y' . However, it is clearly present in the orange plot, where it should be forbidden. This is explained because the nanotree does not have only $\{100\}$ crystalline planes but a more complex structure that allows TO mode for any input polarization. In other words, this is the proof that the nanotree grows in a "fake" [100] direction, in accordance with the TEM study in section 2.3.

Chapter 4

Photoluminescence and cathodoluminescence

Photoluminescence and cathodoluminescence spectroscopies are two contactless techniques useful to assess semiconductor crystals. Both require the excitation of the material, creating and electron-hole pair and observing its recombination. Defects on crystals may create intermediate emission levels that are detected, thus revealing imperfections of the crystalline structure. This chapter aims to explain the physical phenomenas that occur in this processes and explain the results obtained on nanotrees accordingly.

4.1 Band theory

Solid state physics describe conduction in materials with band theory. Although this model may be of complex application in certain materials, such as single molecule or organic semiconductors, it is valid for crystalline semiconductors with a high number of atoms. When a set of atoms is arranged together, their atomic orbitals overlap. Due to the exclusion principle for electrons, each atomic orbital splits, forming a discrete set of states that, due to its proximity in energy, can be considered as a continuous band. Solving the Schrödinger equation for an electron in a periodic potential gives solutions in the form of waves, which are called Bloch functions. From this solutions, a set of allowed and forbidden energies arise. The allowed states forming bands are separated by a prohibited energy span named bandgap. The allowed levels below this bandgap are called valence band, while the states with energy above this bandgap are called conduction band. At T = 0 K, valence band is fully occupied, while conduction band is empty. If energy is transferred to an electron, it can eventually cross the bandgap and occupy a state in the conduction band. This process also lets a space in the valence band named "hole". An electron-hole pair has been created. The electron can occupy any of the states in the conduction band, depending on the energy that it gained to perform the transition. This electron may eventually lose its energy by falling into a lower energy state. If it crosses the bandgap and falls in the valence band again, the hole that has been previously created disappears. This is called an electron-hole recombination.

To satisfy energy conservation, this process may arise to the creation of either a photon, a phonon or a combination of them. If the process involves the creation of a photon it is said to be a radiative recombination, while if the process involves only phonons it is said to be non-radiative. Non-radiative recombination is an undesired process since it depletes the optoelectronical properties of the material. In a semiconductor, if the maximum in energy of the valence band and the minimum in energy of the conduction band are characterized by the same wavevector, it is said to have a direct bandgap. For direct bandgap materials, excited electrons can recombine releasing their energy by the creation of a photon. However, in indirect bandgap materials, a recombination process must involve also a phonon to satisfy momentum conservation. This makes this process much less likely to occur. For this reason, direct band gap semiconductors show more interesting optical properties.

The material studied during this thesis, *GaAs*, is a direct bandgap semiconductor, whose bandgap energy can be fitted as a function of temperature [20] to:

$$E_g = 1.519 - \frac{5.405 \cdot 10^{-4} \cdot T^2}{T + 204}(eV) \tag{4.1}$$

4.2 Measurements on nanotrees

The theory explained above stands for bulk semiconductors with a perfect mono crystalline structure. However, inhomogeneities in crystals, such as strain, twins and surfaces, create levels which may lie inside the bandgap. This gives rise to new recombination paths that, if they are radiative, are reflected in a red-shifted photon emission.

Due to the fact that nanotrees have intrinsically a penta-twin, as seen in figure 2.4, with a polarity inversion in one of the boundaries, it is reasonable to expect emission from levels related with this defects. Moreover, most of the non-radiative recombination occurs at the surface. Due to the large area to volume ratio of the nanotree, this becomes a problem to observe photoluminescence. To prevent surface recombination, the nanotree is passivated with an *AlGaAs* shell of around 30 nm thick. Thanks to this, a type-I band alignment is created in the heterojunction which traps the carriers inside the *GaAs* core and prevents recombination at surface. An outer *GaAs* shell is grown to prevent oxidation of *AlGaAs* [21]. With this, photon emission is dramatically enhanced.

4.2.1 Photoluminescence

The setup used for photoluminescence (PL) is similar to the one used for Raman spectroscopy. By means of a 523 nm Ti:Shappire laser focused with an objective lens that allows μm resolution, the sample is excited. Note that the used wavelength corresponds to a photon energy larger than the bandgap.

Thanks to this fact, photons are absorbed and electron-hole pairs are created. When they recombine, they may emit a photon that is collected with the objective lens and sent to an spectrometer. In comparison with Raman spectroscopy, the power used to excite the sample can be much lower, since Raman shift is an inelastic effect that is less likely to happen, thus leading to a lower signal intensity.

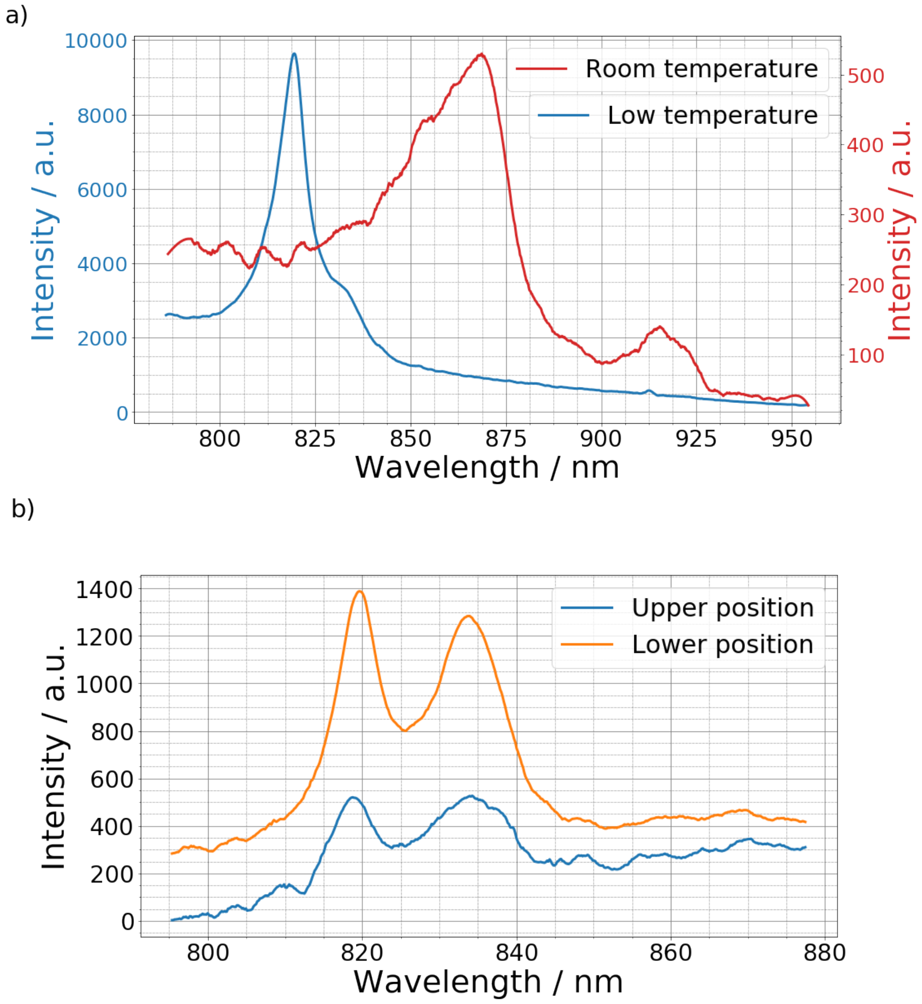

FIGURE 4.1: Photoluminescence spectra on a nanotree lying on *Si* substrate. Plot a) shows high power measurements (300 μW) for RT and LT. Plot b) shows low power measurements (30 μW) at LT for two different zones of the nanotree. Spectras are shifted vertically for a better visualization.

By examining the data from the spectrometer, an inside view of the energy levels on the nanotree is obtained. Figure 4.1a shows room temperature (RT, 293 K) and low temperature (LT, 12 K) photoluminescence measurements. As it can be seen, for room temperature, which corresponds to the red plot, the main peak stands at 868 nm (1.43 eV), while for the low temperature it stands at 819 nm (1.51 eV). In both cases, this is in perfect accordance with equation 4.1 and indicates that these peaks come from the bandgap emission. However, the room temperature peak is less intense and it has a blue-shifted tail.

Aversely, for the low temperature, the peak is symmetric and more intense. The blue-shifted tail of the RT plot comes from emission above the bandgap. Due to thermal energy, the population of levels above the bandgap is larger, and thus larger energy radiative recombinations appear. At low temperature, all excited electrons occupy the less energetic levels of the conduction band, leading to a symmetric and sharp emission. An increase in the intensity of the signal as temperature is lowered has been previously observed and explained in literature [22]. At low temperature, electron-hole pairs are binded in what is called an exciton, with a binding energy of the order of meV. Thermal energy fluctuations of the order of kT are not enough to dissociate this state at LT. As the temperature increases, so it does the thermal energy, being enough to dissociate this exciton and allowing non-radiative recombination paths for the carriers. The presence of a peak both for RT and LT at around 915 nm is attributed to the substrate or to an artifact in the instrument, since it is also observed away from the nanotree. Furthermore, LT plot shows a small unknown peak at 834 nm. To assess this peak, very low power measurements were made at LT. Figure 4.1b shows the results of this measurements for two different positions in the tree, one near the top and one near the bottom. Interestingly, it is clearly seen that the ratio between the bandgap peak (819 nm) and the unknown peak (834 nm) is not kept constant from high power to low power measurements. The height of the unknown peak with respect to the bandgap peak increases as the power decreases. This is explained because this peak belongs to a level with low density of state available. At low power, the electron-hole creation is small and this level can host the carriers that are created. At higher powers, the number of carriers increases and saturates this unknown level. Conversely, the conduction band has virtually unlimited states to be filled, so it can host unlimited carriers. For this reason, as the power increases, the bandgap peak increases while the unknown peak reaches a ceiling of emission. This saturable level may be attributed to two things. Firstly, it has been observed in previous works that this peak may come from carbon contamination in *GaAs* [23]. Carbon acts as an acceptor dopant creating a level near the valence band that matches perfectly the emission observed. Secondly, this unknown peak may be attributed to intermediate levels inside the bandgap created by the crystalline defects, such as the central twin or the polarity inversion.

Despite all of this, the bandgap emission is sharp (FWHM = 6 nm at LT), which indicates that recombination paths created by imperfections are minor and the overall optoelectronic properties of the nanotree are fairly good. Photoluminescence gives a good spectral resolution but a poor spatial resolution, limited by the size of the laser spot near the diffraction limit of light. To have a deeper understanding on the spatial resolution of luminescence on nanotrees a further technique is needed: cathodoluminescence.

4.2.2 Cathodoluminescence

The physics underlaying behind cathodoluminescence (CL) is very similar to photoluminescence. Its main objective is to analyze the emission spectra and relate it to its band characteristics. However, in cathodoluminescence, the excitation of the sample is made by means of an electron beam. Due to the fact that electron wavelength is smaller that light wavelength, the excitation with electrons permits a higher spatial resolution. In other words, photoluminescence gives an overview of nanotree emission, while with cathodoluminescence the spectra can be related to particular positions in the nanotree.

Measurements were performed with an Attolight CL-SEM Grammont 2172. This instrument uses the electron gun both to excite the sample and to obtain SEM images of it.

Figure 4.2a shows an intensity map of the emission around 870 nm for a measurement at RT. Interestingly, an elongated region with lower emission can be seen at the center of the nanotree. This is attributed to the effect of the twin that follows [100] direction discussed in section 2.3, which acts as a non-radiative recombination center. The spectra shown is obtained at a particular point of this scan. Unfortunately, the high electron gun tension needed to obtain signal (up to 5 kV) makes the main bandgap peak to broaden with respect to PL. In fact, it overlaps with the unknown peak at 834 nm found during PL, so CL does not unveil any extra information regarding this. Besides, this high electron tension impinging locally the nanotree induces a charge on it that deflects the electron beam and thus drifts the image. This is the cause of the deformed shape in figure 4.2a. When the electron gun is shut down the charge is dissipated through the substrate and the image recovers the shape of the nanotree.

At LT the scenario is different. Due to the decrease in temperature, diffusion length of carriers increases [20]. This means that carriers can travel far from the point where they were generated. For this reason, there are more chances that carriers approach the central twin at some point during their diffusion. At RT, only carriers generated near the twin can reach it, and thus only the pixels near the twin have a low intensity. In other words, the twin only affects to carriers generated at the neighbor of it. Notice that the instrument excites carriers at a determinate pixel but detects the emission of the whole surface and links it to the pixel where it was excited. At LT, the twin affects to carriers generated everywhere and for this reason the LT map does not show a dark area at the center. More interestingly, the map in figure 4.2b shows intensities for two different wavelengths, which are 819 nm (green tonality) and 670 nm (red tonality). Emission at 670 nm is attributed to *AlGaAs* shell. As it can be seen, it is enhanced at the top of the nanotree, where the thickness of the *GaAs* core is smaller. Lastly, the unknown peak at 834 nm found in PL can not be attributed to any region of the nanotree, thus empowering the hypothesis that it comes from carbon contamination.

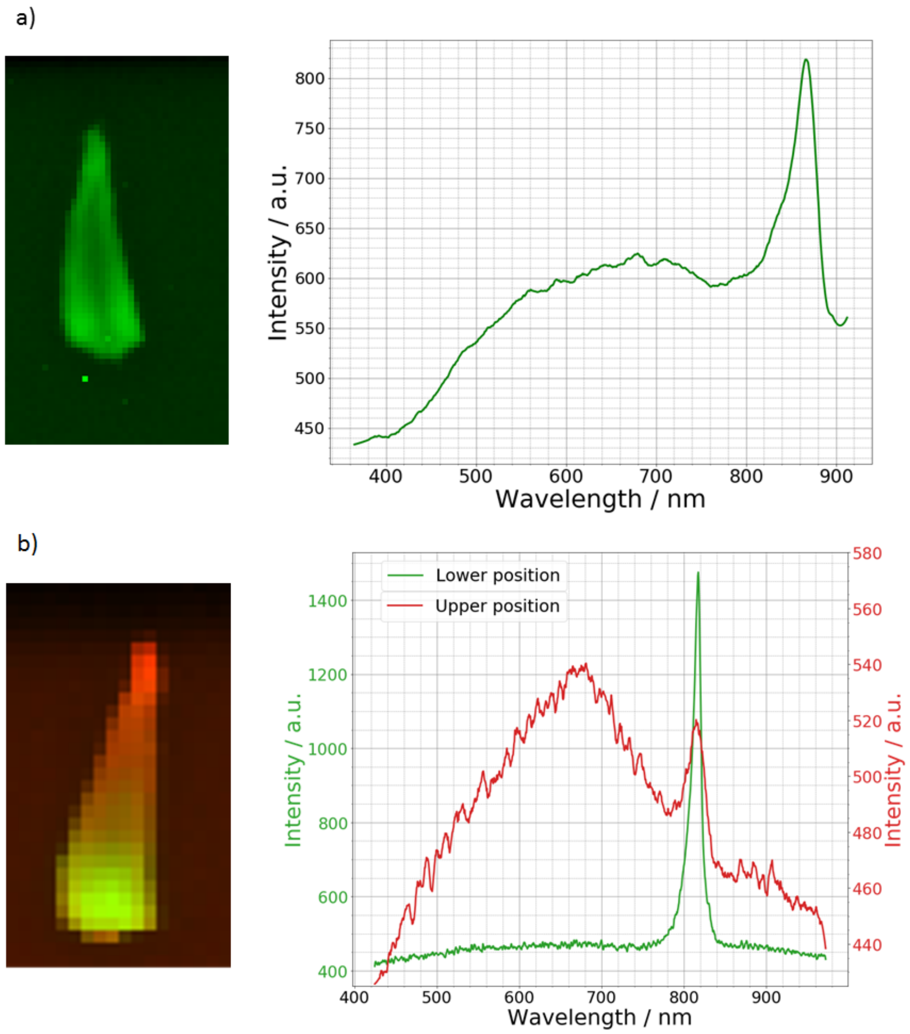

FIGURE 4.2: Cathodoluminescence mapping on nanotrees. Plot a) shows RT spectra at a point near the base of the nanotree. Plot b) shows LT spectra at different positions on the nanotree. Measurements were taken at an acceleration voltage of 5 kV.

Chapter 5

A step towards functional devices

Once the optical characterization of *GaAs* nanotrees is done, it is time to give a functionality to them. Many possibilities can be imagined, from solar cells to single photon detectors. This chapter aims to explore the future of nanotrees and state a path to obtain functional devices with them.

5.1 Nanotree solar cells

Thanks to its direct bandgap, *GaAs* shows outstanding properties for solar cells. However, as discussed in the introduction, *GaAs* is scarce, and a bulk device with low environmental footprint would be impossible to implement. Nanowires help to solve this problem by reducing the amount of material needed to make a device. The elongated shape of nanowires makes them act as a waveguide. For standing nanowires, the effect of guiding modes enhances light confinement inside the semiconductor, leading to higher a absorption [24]. Furthermore, the fact that nanowires are grown in an array with a certain pitch distance between them allows resonant interactions that enhance absorption even more [25].

A function of merit named absorption efficiency can be defined as the cross-section absorption divided by the projected area of the nanowire. Absorption efficiency for bulk semiconductors is always ≤ 1. On the contrary, in nanowires it is possible to have absorption efficiencies ≥ 1 [24]. Thus, in comparison, less material is needed in a nanowire with respect to a planar solar cell for a similar absorption. Unlikely the work presented in [24], for nanotrees the absorption wavelengths depend strongly on the length of the structure. However, as simulations in appendix A reveal, nanotrees own very good confinement properties. For a solar cell, it is desirable to have a broad band of absorption. Thanks to their tapered shape, nanotrees show fairly good behavior in this sense. For a 1450 nm long nanotree, wavelengths between 600 nm and 700 nm are strongly enhanced, as seen in figure A.4. However, further simulations need to be developed in order to have a reliable comparison with [24].

Of course, to obtain a solar cell it is not enough to have only an intrinsic semiconductor absorber, but also selective contacts to extract carriers from it. Here, a method to obtain solar cells out of nanotrees will be explained, although it is not planned to be tested in a near future.

This time the process starts with a highly n-doped *Si* wafer. A metal deposition is made in one side of the wafer, which will be the lower part. On the upper side, pillars are patterned on the wafer following the top-down approach described in section 2.1. After, the sample is introduced in the MBE for normal growth of intrinsic *GaAs* by VLS. Once the nanotree core is completed and the self-catalyzer droplet is extincted, the chamber conditions are switched to allow radial growth by lowering the substrate temperature. By introducing a dopant, such as *Si* or *C*, a p-type *GaAs* shell is grown. Before contacting the upper part, a layer of Su-8 isolating photoresist is spin-coated to prevent a possible undesired contact between the upper electrode and the solar cell layers. If needed, this photoresist can be etched to cover only the lower part of the nanotree. Finally, an Indium Tin Oxide (ITO) layer is spin coated, which is a transparent and conductive material that will extract the carriers.

With this procedure the basic items to obtain a solar cell are included. On one hand, an absorbing material, which is the intrinsic *GaAs* core. On the other hand, n and p type layers surrounding this intrinsic core, that will act as selective contacts for electrons and holes. As the light impinges the core, electron-hole pairs are generated. Due to the reduced dimensions of the nanotree, of the order of the diffusion length, and the built in potential generated by the p-i-n junction, carriers will approach the selective contacts. Electrons will flow towards the pillar. At this point, the n-doped layer will allow this electrons to cross to the metal contact and at the same time will block the holes, acting as an electron transport layer. In the same way, holes will flow towards the outer p-doped shell, which will not allow electrons to cross, acting as a hole transport layer. Thanks to this, carriers are created and separated, thus generating current.

Of course, this is only a rough orientation on how a nanotree solar cell would work. Further study needs to be done in order to bring this to reality.

5.2 Quantum dots in nanotrees

Next step in this work will be to build quantum dots inside nanotrees. This section will describe the steps that will be taken during next month after the thesis submission deadline. For this reason, own experimental results can not be shown.

5.2.1 Zero-dimensional confinement

Quantum dots are tiny semiconductor particles, about tenths of nanometers of diameter, that show unique electronic properties thanks to its large surface to volume ratio. Indeed, they behave halfway between bulk semiconductors and single molecules, opening a wide range of possibilities for optoelectronic applications.

From an energetic point of view, quantum dots are formed by electrons trapped in a potential well. It is said that they are confined in zero dimensions. By solving Schrödinger's equation for a spherical potential well [26], one can obtain that the energy of a particle inside this potential well is quantized and its difference with bulk band gap is

$$\Delta E = \frac{\hbar}{2m_r}\left(\frac{\pi}{R}\right)^2 \tag{5.1}$$

where m_r is the reduced electron-hole mass and R is the radius of the spherical potential well that models the quantum dot. Note that this derivation implies that the modeled quantum dot is somehow spherical, which it will be shown that it is not true in the next section. This equation indicates that the confinement induced energy shift is inversely proportional to R^2. This means that smaller quantum dots will have an energy between the ground and the excited state larger than the equivalent bulk bandgap. As the quantum dot increases in radius, the energy shift decreases, approaching bulk properties. This implies that the emission wavelength of the quantum dot can be tuned by its size, which turns out to be a very interesting property and is the reason why quantum dots are a central topic in nanotechnology.

This section presents two methods for self-assembling of quantum dots in nanotrees that has already been performed by other groups. During next month after the thesis submission deadline this will be the topic to focus. For this reason, experimental results regarding quantum dots can not be included in this document.

5.2.2 Quantum dots by aluminum segregation

After the *GaAs* nanotree core, aluminum is introduced in the MBE chamber to grown an outer shell. Some of the *Ga* places in the lattice are substituted by *Al* giving rise to an alloy named $Al_xGa_{1-x}As$, where x is a number between 0 and 1 that indicates the *Al* composition. This alloy has a very similar lattice constant than *GaAs*, which makes epitaxial growth very favorable. Unlikely the shell for luminescence enhancement in section 4.2, this time the shell is much more thicker, around 100 nm. During the deposition of this layer, *Ga* and *Al* adatoms compete for placing themselves in the most energetically favorable facets, this is, the facets with a lower chemical potential [27]. However, stronger surface diffusion of *Ga* with respect to *Al* helps *Ga* to reach this most favorable facets first, and thus accumulate there. Of course, entropy of mixing causes an increase of the chemical potential for *Ga* adatoms at this facets, hindering *Ga* diffusion and enhancing *Al* diffusion towards this facets [28]. This two opposing effects compete giving rise to a segregation of *Al* at certain regions. Figure 5.1a shows an scheme of this segregation in an hexagonal nanowire. A dark blue radial planes, which correspond to areas with high *Al* content, appear along the nanowire at the vertices of the hexagon. More interestingly, it has been observed in [29] that this radial planes may eventually bifurcate at some points, creating areas of low *Al* content represented with red color. Figure 5.1b shows an aberration-corrected high-angle annular dark-field STEM image of the cross-section of a real *GaAs* nanowire. The different colors represent areas with different *Al* content. The bifurcation of the *Al* rich lines can be seen, forming a triangular cross-section along by $\{211\}$ planes. In the center, a triangular region with low Al content. Figure 5.1c shows the band diagram of this setup. An area of low Al content surrounded by an area of high Al content creates a potential well for the carriers. As discussed in the previous section, this quantum well brought to three dimensions creates a quantum dot.

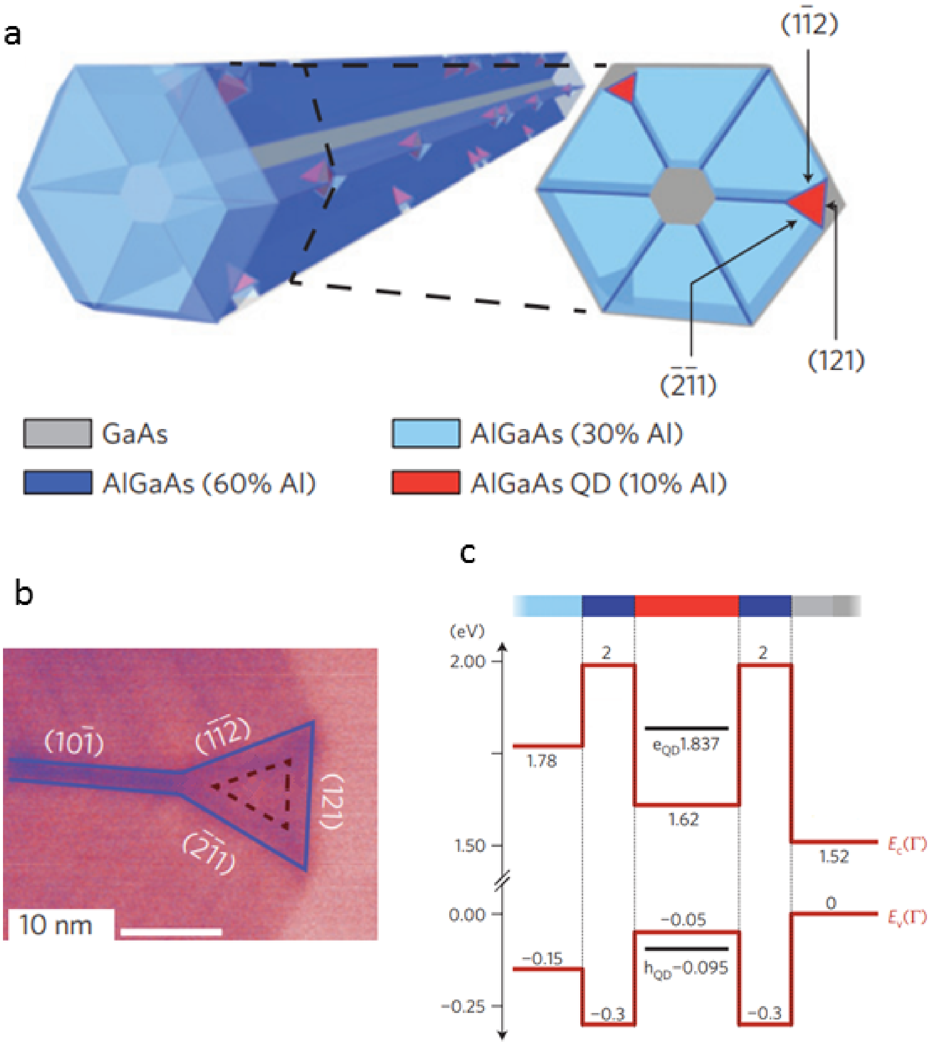

FIGURE 5.1: Formation of quantum dots by aluminum segregation in an hexagonal cross-section nanowire. Extracted and adapted from [29].

As a last step, before extracting the sample from the MBE, an outer $GaAs$ shell is grown to prevent oxidation of the $AlGaAs$ layer and the subsequent damage of the quantum dots.

The presence of quantum dots will be proved firstly by photoluminescence. Accordingly to previous works, peaks around 650 nm arising from the quantum dots are expected. However, as the bifurcations appear randomly, and so does the quantum dots, it is necessary to use cathodoluminescence to have spatially-resolved emission map of the nanotree.

5.2.3 Stranski–Krastanov *InAs* quantum dots

In the previous method, quantum dots appear randomly along the nanotree. There is no way to obtain the dots in certain places. The method purposed in this section aims to build quantum dots on the surface of the silicon pillar and after, grow nanotree on them. *InAs* quantum dots on a [100] *Si* wafer has been previously obtained. Without any strain, *InAs* band alignment with *Si* is of type-II, which means the following. The conduction band of *InAs* is shifted downwards with respect to the conduction band of *Si*, thus creating a well for electrons. For the valence band, *InAs* is also shifted downwards with respect to the *Si* valence band, which implies that holes are not accumulated in *InAs*. However, if a strain is applied to the *InAs*, the bands realign with an upward shift of the *InAs* valence band above the *Si* valence band [7]. This indeed forms a quantum well both for electrons and holes.

The process starts with the pillar patterning on the substrate and is exactly the same than the one described in section 2.1. After, the substrate is introduced in the MBE and heated to a temperature of 250°C to start deposition of *InAs*. Due to the strong lattice mismatch between *InAs* and *Si*, it is not expected to grow in perfect monolayers, but forming small island or clusters of *InAs*, united by a wetting *InAs* layer of a few Angstroms. This type of growth is known as Stranski-Krastanov. Thanks to it, it is expected to obtain a tapestry of *InAs* islands of similar sizes that, because of the band alignment explained above, will form quantum dots.

To prove the existence of quantum dots, photoluminescence will be done. As the quantum dots are expected to grow in all the pillars, it is not necessary to have a high spatial resolution of the emission spectra, and for this reason cathodoluminescence will not be used. Accordingly to previous works, it is expected to obtain peaks at 1.3 μm arising from the quantum dot emission.

After, nanotrees will be grown on top of the pillars. The reason for that is the following. Quantum dots have outstanding photon emission/absorption yields. However, the coupling of the light with the environment (the extraction or injection of photons) is very difficult due to the high refractive index of the semiconductor that forms the quantum dot [30]. To overcome this problem, it is necessary to embed the quantum dot in a structure with a similar refractive index and that can properly couple light with the environment: nanotrees. As discussed in Appendix A, nanotrees show a very good light confinement, specially at the base, where the quantum dots are formed, enhancing the electric field in this area. Furthermore, band alignment between *GaAs* and *InAs* is of type-I, meaning that the conduction band of *InAs* is downwards the conduction band of *GaAs*, and the valence band of *InAs* is upwards the valence band of *GaAs* [31]. This gives rise, again, to a well for the carriers inside the *InAs* quantum dot.

But growing nanotrees on this *InAs* quantum dots is still more challenging. As discussed in chapter 2, the triggering of the formation of nanotrees is tightly related with the surface of the *Si* pillar and the droplet contact angle. In the current scenario, this parameters change completely. So far, the understanding of the growth is not sharp enough to make any prediction on how this change will affect the nanotrees. It is expected to try this experimental growth by the end of July 2018.

5.3 Their future is bright

The fact that nanotrees can host quantum dots and confine incident light at customized wavelengths, as discussed in appendix A, makes them a promising choice for photonic devices. Optical communications use wavelengths from 1260 nm to 1625nm. Particularly, O-band (from 1260 nm to 1360 nm) and C-band (from 1530 nm to 1565 nm) are the most commonly used due to the minimum absorption of optic fibers at those wavelengths. Stranski-Krastanov *InAs* quantum dots are expected to have a transition in this range of energies. By tuning the growth characteristics it is expected that the exact emission wavelength can be adapted to this communication bands. Furthermore, depending on the size of the nanotree, the best confined wavelength can be tuned. Simulations have predicted that, for a 1300 nm wavelength confinement the nanotree must be around 3000 nm in length, which lies in the range that can be achieved with the method described in this work. Bulgarini describes in his thesis [32] a method to obtain single-photon detectors with quantum dots in nanowires. By contacting a nanotree with a procedure similar to the one described in section 5.1 and applying a bias voltage, the setup would act as an avalanche photodiode, allowing very precise photon counts. In the same way, quantum dots can also act as single-photon sources. Considering a quantum dot as a two-level system [33] that can host two electrons in each level, one spin up and one spin down, it has been proved that they provide two recombination paths that can produce polarization entangled photons [34]. Thanks to the nanotree, photons could be extracted and coupled to a waveguide. This may have a clear application in quantum communication, where information is stored in the polarization of the emitted photons.

Overall, this work stated a method to obtain vertical *GaAs* nanowires on [100] *Si* without a catalyzer. This is the first time that was achieved and the resulting structures were named nanotrees. A deep insight into this nanotrees was taken by using optical techniques such as Raman spectroscopy or photo and cathodoluminescence. With the results of this measurements it was proved that nanotrees are promising for devices. An overview of the potential applications for nanotrees, which span from energy harvesting to quantum photonics, was exposed. However, the low yield of nanotrees sets a practical limitation. From now on, the work will be focused on improving this yield by changing the growth parameters and the array characteristics. In parallel, heterostructures will be grown in order to obtain quantum dots. Although the path to achieve functional devices with nanotrees is still long, the basis has already been settled.

Appendix A

Lumerical Simulations

Lumerical is a widely known software used for photonic and photoelectronic simulations. Models in this work were performed following two goals. The first goal was to find the optimal setup for a maximum light absorption in the nanotree. This was useful to enhance the Raman and photoluminescence signal. The second goal was to understand light confinement in a standing nanotree in order to explore the possibilities of coupling light for functional devices.

A.1 Finite-difference time-domain

Light propagation in space is governed by the well-known Maxwell's equations, which depend on time and space. To solve this equations, the software divides the space in small but finite regions which conform what is called the mesh. The equations are discretized for each finite element in space and solved for each time step. With this it is obtained the evolution of the electric and magnetic field in the simulation region. This method requires all the simulation space to be meshed and this grid must be fine enough compared to the wavelength of the propagating light and the object in order to resolve the equations accurately. For this reason, very long computation times (up to 8 hours) must be expected. Two different setups are used. In the first one, which emulates the position of the nanotree during Raman and photoluminescence measurements, the nanotree is laying on a silicon substrate. The Si substrate has a very thin SiO_2 layer, around 10 nm, that corresponds to the native oxide of the wafer where nanotrees are transfered. The second setup aims to emulate the position of the nanotree standing on the Si pillar, as it would be in a functional device. Both setups can be observed in figure A.1.

In order to optimize the computation time, a fine mesh of 2 nm is defined around the nanotree while in the rest of the computational space the mesh gets thicker as it moves away from the nanotree. An incident wave is simulated by means of a total-field scattered-field (TFSF) source. In TFSF sources, the incident field is a planar wave with wavevector normal to the injection surface, which in this case is the upper one. As the wave propagates, some of the power is scattered and some is not. When the wave arrives to the end surface, the non-scattered field is subtracted. In this way, the scattering properties of the nanotree are observed. Perfectly Matching Layer (PML) boundary conditions are used, which means that they absorb light waves

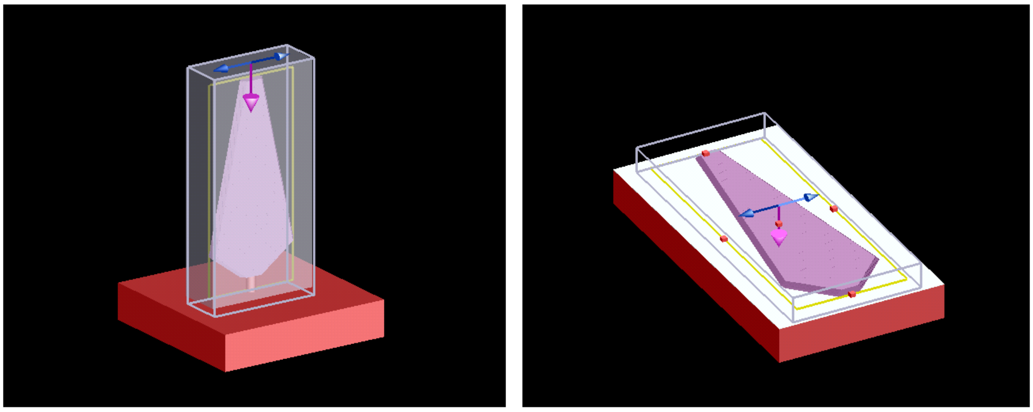

FIGURE A.1: Perspective view of the two setups used for Lumerical simulations. The purple and blue vectors indicate the wavevector and the polarization of the incident light, respectively. The monitor is represented as a yellow rectangle.

with minimal reflections. To observe the electric field during the simulation, a two-dimensional frequency-domain field profile monitor is placed inside the nanotree. This monitor collects and integrates the intensity of the electric field during the simulation time.

A.2 Results and discussion

For a standing nanotree, different lengths were tested. Figure A.2 shows a map of the intensity of the electric field in a nanotree of 1050 nm long. As it can be seen, incident light polarized along $\vec{x}$ is properly confined. Figure A.3 shows two cross-section monitors for a simulation at 520 nm. Two different modes can be observed at different heights. As expected, confinement is dependent on the wavelength. An optimum light confinement is obtained at 570 nm for this size. Interestingly, if the polarization of the incident light is set along $\vec{y}$ axis, the light is not confined, although no figures are shown in this case. For longer nanotrees, it was found out, as expected, that they could properly confine longer wavelengths. Figure A.4 shows the same simulations for a 1450 nm long nanotree. Optimum confinement is found for 622 nm. In the same way, figure A.5 shows two different modes that are hosted inside the nanotree at 622 nm.

For laying nanotrees the scenario is completely different. Firstly, the dependence on the wavelength is less strict. It was found out that a fairly good intensity inside the nanotree was achieved for 532 nm wavelength. For this reason, this was the light used for excitation in Raman spectroscopy. Additionally, it was found that there is no dependence on the incident polarization.

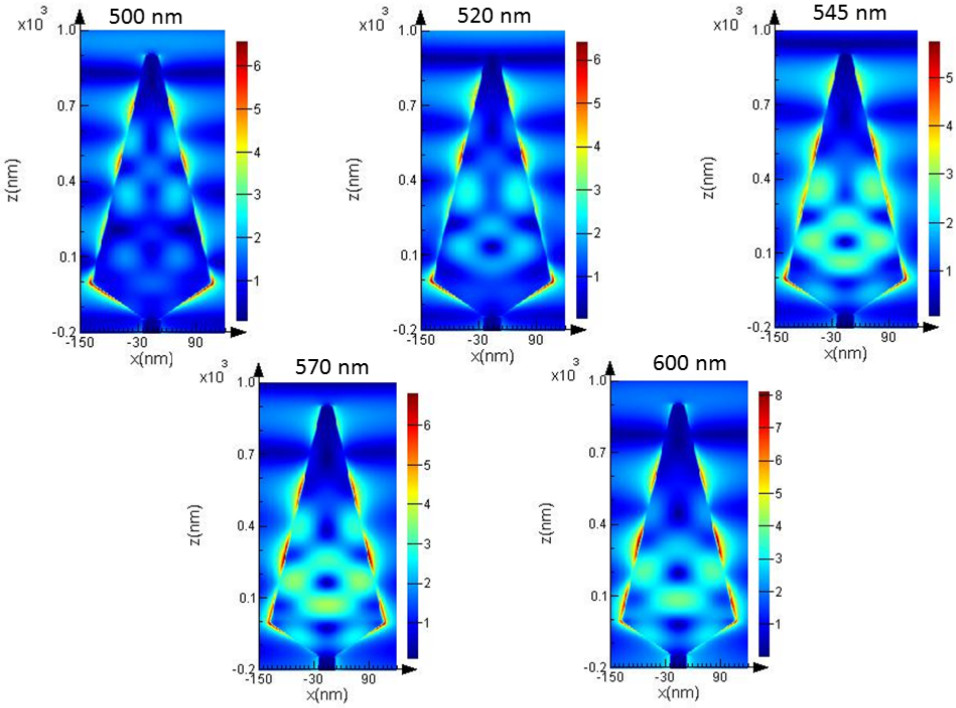

FIGURE A.2: Electric field intensity map for an incident $\vec{z}$ wave polarized along $\vec{x}$ in a 1050 nm nanotree.

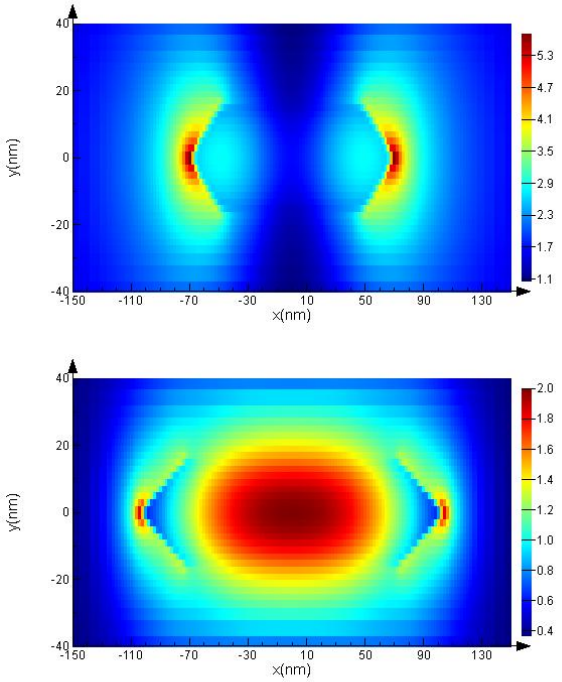

FIGURE A.3: Cross-section electric field intensity map for an incident 520 nm $\vec{z}$ wave polarized along $\vec{x}$ in a 1050 nm nanotree for two different positions.

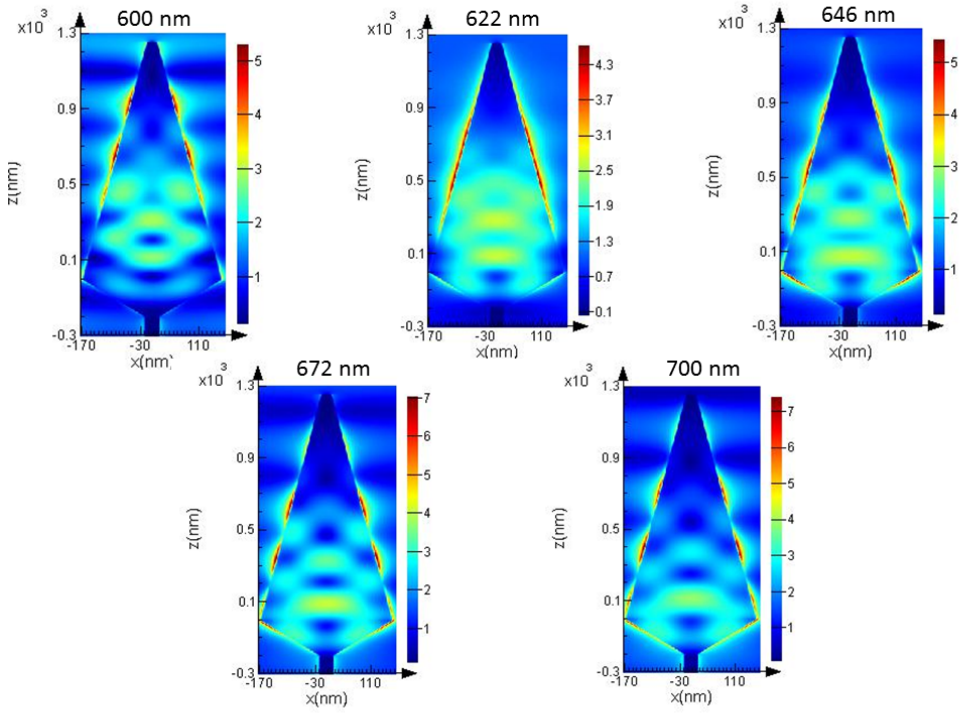

FIGURE A.4: Electric field intensity map for an incident $\vec{z}$ wave polarized along $\vec{x}$ in a 1450 nm nanotree.

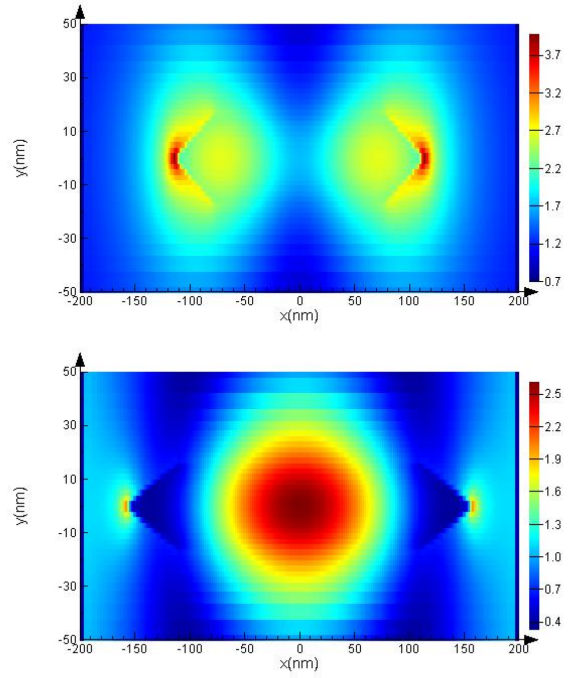

FIGURE A.5: Cross-section electric field intensity map for an incident 622 nm $\vec{z}$ wave polarized along $\vec{x}$ in a 1450 nm nanotree for two different positions.

Bibliography

[1] M. De La Mata, X. Zhou, F. Furtmayr, J. Teubert, S. Gradečak, M. Eickhoff, A. F. i Morral, and J. Arbiol, "A review of mbe grown 0d, 1d and 2d quantum structures in a nanowire," *Journal of Materials Chemistry C*, vol. 1, no. 28, pp. 4300–4312, 2013.

[2] P. Krogstrup, H. I. Jørgensen, M. Heiss, O. Demichel, J. V. Holm, M. Aagesen, J. Nygard, and A. F. i Morral, "Single-nanowire solar cells beyond the shockley–queisser limit," *Nature Photonics*, vol. 7, no. 4, p. 306, 2013.

[3] D. Saxena, S. Mokkapati, P. Parkinson, N. Jiang, Q. Gao, H. H. Tan, and C. Jagadish, "Optically pumped room-temperature gaas nanowire lasers," *Nature Photonics*, vol. 7, no. 12, p. 963, 2013.

[4] S. M. Frolov, S. R. Plissard, S. Nadj-Perge, L. P. Kouwenhoven, and E. P. Bakkers, "Quantum computing based on semiconductor nanowires," *MRS bulletin*, vol. 38, no. 10, pp. 809–815, 2013.

[5] M. Björk, B. Ohlsson, T. Sass, A. Persson, C. Thelander, M. Magnusson, K. Deppert, L. Wallenberg, and L. Samuelson, "One-dimensional heterostructures in semiconductor nanowhiskers," *Applied Physics Letters*, vol. 80, no. 6, pp. 1058–1060, 2002.

[6] K. A. Dick, "A review of nanowire growth promoted by alloys and non-alloying elements with emphasis on au-assisted iii–v nanowires," *Progress in Crystal Growth and Characterization of Materials*, vol. 54, no. 3-4, pp. 138–173, 2008.

[7] G. Cirlin, V. Dubrovskii, V. Petrov, N. Polyakov, N. Korneeva, V. Demidov, A. Golubok, S. Masalov, D. Kurochkin, O. Gorbenko, *et al.*, "Formation of inas quantum dots on a silicon (100) surface," *Semiconductor science and technology*, vol. 13, no. 11, p. 1262, 1998.

[8] C. of MicroNanotechnology, 2017. `https://cmi.epfl.ch/`.

[9] R. Wagner and W. Ellis, "Vapor-liquid-solid mechanism of single crystal growth," *Applied Physics Letters*, vol. 4, no. 5, pp. 89–90, 1964.

[10] Q. Qin, S. Yin, G. Cheng, X. Li, T.-H. Chang, G. Richter, Y. Zhu, and H. Gao, "Recoverable plasticity in penta-twinned metallic nanowires governed by dislocation nucleation and retraction," *Nature communications*, vol. 6, p. 5983, 2015.

[11] S. L. Thomas, A. H. King, and D. J. Srolovitz, "When twins collide: Twin junctions in nanocrystalline nickel," *Acta Materialia*, vol. 113, pp. 301–310, 2016.

[12] C. L. Johnson, E. Snoeck, M. Ezcurdia, B. Rodríguez-González, I. Pastoriza-Santos, L. M. Liz-Marzán, and M. J. Hÿtch, "Effects of elastic anisotropy on strain distributions in decahedral gold nanoparticles," *Nature materials*, vol. 7, no. 2, p. 120, 2008.

[13] C. of MicroNanotechnology, 2017. `https://cmi.epfl.ch/metrology/Nova600/Nova600_Home.php`.

[14] C. Kittel, P. McEuen, and P. McEuen, *Introduction to solid state physics*, vol. 8. Wiley New York, 1996.

[15] F. Amaduzzi, "Functional properties of iii-v nanowires addressed by raman spectroscopy," tech. rep., EPFL, 2017.

[16] Y. Peter and M. Cardona, *Fundamentals of semiconductors: physics and materials properties*. Springer Science & Business Media, 2010.

[17] I. Zardo, S. Conesa-Boj, F. Peiro, J. Morante, J. Arbiol, E. Uccelli, G. Abstreiter, and A. F. i Morral, "Raman spectroscopy of wurtzite and zinc-blende gaas nanowires: polarization dependence, selection rules, and strain effects," *Physical review B*, vol. 80, no. 24, p. 245324, 2009.

[18] D. Spirkoska, G. Abstreiter, and A. F. i Morral, "Size and environment dependence of surface phonon modes of gallium arsenide nanowires as measured by raman spectroscopy," *Nanotechnology*, vol. 19, no. 43, p. 435704, 2008.

[19] N. Begum, M. Piccin, F. Jabeen, G. Bais, S. Rubini, F. Martelli, and A. Bhatti, "Structural characterization of gaas and inas nanowires by means of raman spectroscopy," *Journal of Applied Physics*, vol. 104, no. 10, p. 104311, 2008.

[20] I. Institute, 2017. `http://www.ioffe.ru/index_en.html`.

[21] G. Tütüncüoglu, "The growth and optical properties of iii-v nanostructures grown by molecular beam epitaxy," 2017.

[22] D.-S. Jiang, H. Jung, and K. Ploog, "Temperature dependence of photoluminescence from gaas single and multiple quantum-well heterostructures grown by molecular-beam epitaxy," *Journal of applied physics*, vol. 64, no. 3, pp. 1371–1377, 1988.

[23] G. Tutuncuoglu, M. de La Mata, D. Deiana, H. Potts, F. Matteini, J. Arbiol, and A. F. i Morral, "Towards defect-free 1-d gaas/algaas heterostructures based on gaas nanomembranes," *Nanoscale*, vol. 7, no. 46, pp. 19453–19460, 2015.

[24] S. Mokkapati, D. Saxena, H. H. Tan, and C. Jagadish, "Optical design of nanowire absorbers for wavelength selective photodetectors," *Scientific reports*, vol. 5, p. 15339, 2015.

[25] I. Åberg, G. Vescovi, D. Asoli, U. Naseem, J. P. Gilboy, C. Sundvall, A. Dahlgren, K. E. Svensson, N. Anttu, M. T. Björk, *et al.*, "A gaas nanowire array solar cell with 15.3% efficiency at 1 sun," *IEEE Journal of Photovoltaics*, vol. 6, no. 1, pp. 185–190, 2016.

[26] S. W. Koch *et al.*, *Semiconductor quantum dots*, vol. 2. World Scientific, 1993.

[27] N. Sköld, J. B. Wagner, G. Karlsson, T. Hernán, W. Seifert, M.-E. Pistol, and L. Samuelson, "Phase segregation in alinp shells on gaas nanowires," *Nano letters*, vol. 6, no. 12, pp. 2743–2747, 2006.

[28] G. Biasiol, A. Gustafsson, K. Leifer, and E. Kapon, "Mechanisms of self-ordering in nonplanar epitaxy of semiconductor nanostructures," *Physical Review B*, vol. 65, no. 20, p. 205306, 2002.

[29] M. Heiss, Y. Fontana, A. Gustafsson, G. Wüst, C. Magen, D. O'regan, J. Luo, B. Ketterer, S. Conesa-Boj, A. Kuhlmann, *et al.*, "Self-assembled quantum dots in a nanowire system for quantum photonics," *Nature materials*, vol. 12, no. 5, p. 439, 2013.

[30] M. Pelton, C. Santori, J. Vucković, B. Zhang, G. S. Solomon, J. Plant, and Y. Yamamoto, "Efficient source of single photons: a single quantum dot in a micropost microcavity," *Physical review letters*, vol. 89, no. 23, p. 233602, 2002.

[31] M. Grundmann, O. Stier, and D. Bimberg, "Inas/gaas pyramidal quantum dots: Strain distribution, optical phonons, and electronic structure," *Physical Review B*, vol. 52, no. 16, p. 11969, 1995.

[32] G. Bulgarini, "Nanowire-based quantum photonics," 2014.

[33] P. Senellart, G. Solomon, and A. White, "High-performance semiconductor quantum-dot single-photon sources," *Nature nanotechnology*, vol. 12, no. 11, p. 1026, 2017.

[34] O. Benson, C. Santori, M. Pelton, and Y. Yamamoto, "Regulated and entangled photons from a single quantum dot," *Physical review letters*, vol. 84, no. 11, p. 2513, 2000.